8-2016

An Investigation of Bimodal Cellular Distributions via Supercritical Fluid Assisted (SCF) Foam Injection Molding

Sai Aditya Pradeep
Clemson University, spradee@clemson.edu

AN INVESTIGATION OF BIMODAL CELLULAR DISTRIBUTIONS VIA SUPERCRITICAL FLUID ASSISTED (SCF) FOAM INJECTION MOLDING

A Thesis
Presented to
the Graduate School of
Clemson University

In Partial Fulfillment
of the Requirements for the Degree
Master of Science
Materials Science and Engineering

---

by
Sai Aditya Pradeep
August 2016

Accepted by:
Dr. Srikanth Pilla, Committee Chair
Dr. Gary Lickfield, Committee Member
Dr. Igor Luzinov, Committee Member

ABSTRACT

The Corporate Average Fuel Economy (CAFÉ) standards for 2025 are set to introduce a fleet-wide average of 54.5 MPG for cars and thereby, prevent emissions of 6 billion metric tons of CO_2 [1]. This has propelled the automotive industry to renew their focus on lightweighting cars, particularly through the use of crude oil-based structural foams. While these foams offer a unique combination of ultra-lightweighting with adequate strength, they are practically non-renewable, non-biodegradable and contribute to the growing anthropogenic carbon footprint. An alternative paradigm to such foams is the use of biosourced polymers as they offer immense advantages due to their renewable, sustainable and biodegradable nature.

Currently, polylactic acid (PLA) remains the most abundant commercially consumed biopolymer, but it suffers from two major drawbacks: its inherent brittle nature and poor melt processability. Blending PLA with an inherently toughened counterpart provides an effective mechanism to overcome both these drawbacks [2]. Additionally, foaming of PLA-based blends can provide a replacement for synthetic structural foams. However, processing of such blended foams is inhibited by challenges associated with structural foam molding with regard to controlling foam microstructure – specifically, cell size and cell density. Additionally, controlled processing of bimodal cell structure has remained elusive with currently used molding parameters and chemical blowing agents. Bimodal cellular distributions are preferred for their superior properties – enhanced toughness and compressive strength, weight reduction, and insulating properties – compared to their unimodal counterparts.

This study investigates the effect of material properties and processing parameters on unique cellular distributions of polylactic acid (PLA), polybutylene succinate adipate (PBSA) and their blends processed via supercritical fluid-assisted injection molding. Cell morphology, size and density were determined via scanning electron microscopy, while their influence on mechanical properties was studied using tensile testing. Thermal stability of the blends was studied via differential scanning calorimetry and thermo-gravimetric analyzer. Effect of melt rheology and viscoelastic behavior was studied in an effort to explain the bimodal cellular structure obtained.

ACKNOWLEDGMENTS

At the outset, I express my deep sense of gratitude and sincere thanks to my research advisor, Dr. Srikanth Pilla, for his valuable and inspiring guidance throughout the course of my research at CUICAR. I am indebted for the encouragement and motivation he has shown towards me for exploring new things and his faith in me that has brought a successful completion of the thesis work.

I also take this opportunity to sincerely thank my committee members, Dr. Igor Luzinov and Dr. Gary Lickfield, for their valuable support. I also express my thanks to Prof. Zoran Filipi, Chair & Executive Director of Automotive Engineering and Prof. Rajendra Bordia, Department Chair of Materials Science & Engineering at Clemson University, for ensuring proper functioning of the department facilities which enabled me to pursue my research.

Special thanks are also reserved in particular to Kousaalya Bakthavatchalam, who has been an immense source of support as a friend and as a research colleague. I am grateful to my teachers at CUICAR and Clemson University for having trusted me, constantly motivated me and helped me to build a strong foundation for my future.

Last, and probably the most important, I take this to acknowledge my deepest sense of gratitude and acknowledgement for those because of whom I was able to come here: my family members: Mr. C.N Pradeep and Mrs. Nayana P Hegde No thanks can be enough for the blessings and unconditional love and support of my parents and my sister Sai Pallavi Pradeep, as these have been an important ingredient for my success.

TABLE OF CONTENTS

Page

LIST OF TABLES

LIST OF TABLES (continued)

Table Page

LIST OF FIGURES

LIST OF FIGURES (continued)

LIST OF FIGURES (continued)

Figure Page

LIST OF EQUATIONS

LIST OF SCHEMES

CHAPTER ONE

Introduction

The modern automobile has seen remarkable changes in the types of materials employed in its manufacture. From being a "metallic behemoth" in the 1950s, automobiles have moved towards extensive deployment of alternative lightweight materials over the past few decades. This dramatic shift can be attributed to the increasing demand for lightweighting cars in order to improve fuel economy and meet legislative and regulatory requirements, including those directing automobile manufacturers to increase fuel efficiency and thereby reduce CO_2 emissions in order to combat climate change. In particular, the Corporate Average Fuel Economy (CAFE) standards set by the US Environmental Protection Agency (EPA) [1] set a fleet-wide average of 54.5 MPG for both cars and trucks by the year 2025.

Thermoplastic foams

Thermoplastic foams, as lightweight materials, possess several properties suitable for the automotive sector – high strength-to-weight ratio and acoustic properties, low susceptibility to water vapor, superior impact resistance, and low density. Thermoplastic foams can be categorized based on several criteria, such as cell size, foam structure, foam stiffness, and blowing agents used, as seen in Figure 1.1 [3]. Based on stiffness, these foams can be classified as rigid, semi-rigid and flexible foams. Rigid foams are highly durable and undergo permanent deformation with optimal yield points, rendering them highly effective for load bearing applications. Semi-rigid foams exhibit moderate flexibility and

rigidity as they consist of highly inter-connected cells, making them useful for shock absorbing pads in door trims and sun visors. Flexible foams are mainly used in seat cushions due to their low stiffness and high resilience.

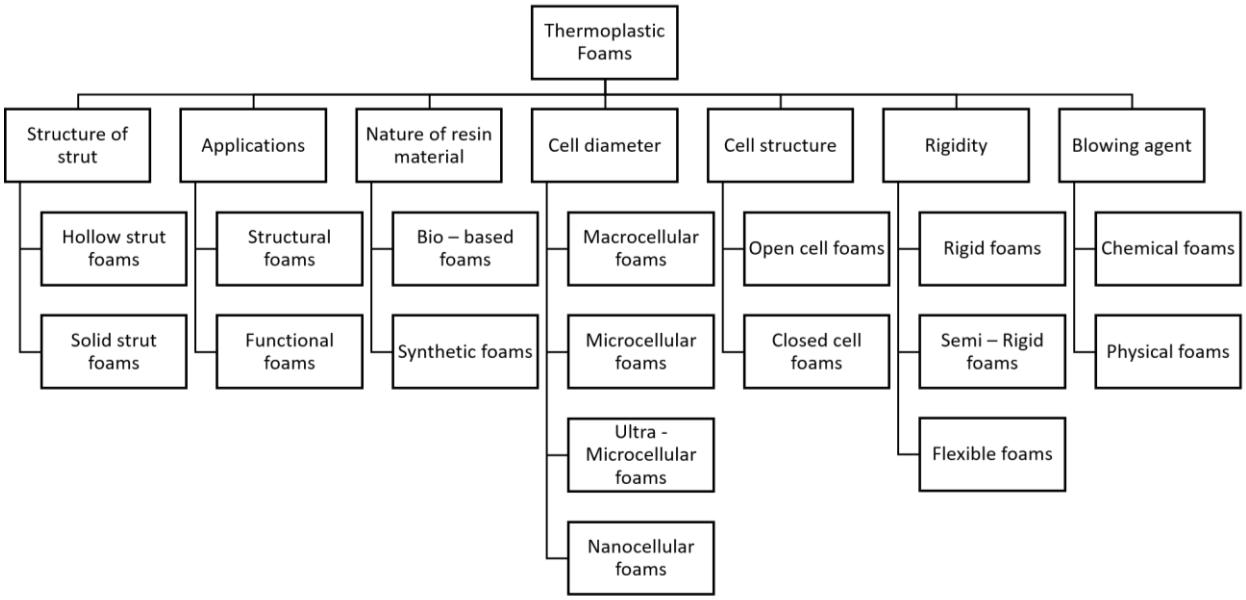

Figure 1.1: Classification of Thermoplastic foams on the basis of various criterion

Thermoplastic foams can also be categorized on the basis of cell size and structure, as this parameter dictates foam properties and applications. Foams are classified as macrocellular, microcellular, ultra-microcellular and nanocellular foams based on their cell diameters (Table 1.1). Differences in cell size of different foams stem from random cell nucleation in the polymer matrix and growth of cells during dispersion of gas. With regard to applications and performance, cell size is believed to be inversely proportional to foam resilience. Table 1.1 details the impact of cell size on foam properties.

Based on the uniformity in cell size, foams are classified as unimodal foams and multimodal foams. Bimodal foams are a subset of multimodal foams, and are defined as

foams with two distinct cell sizes, that is, one size having average cell diameter 5-50% smaller than that of the other.

	Average Cell diameter	Mechanical Strength	Foam density
Macrocellular foams	d > 100 µm		
Microcellular foams	1 µm < d < 100 µm		
Ultra-Microcellular foams	0.1 µm < d < 1 µm		
Nanocellular foams	1nm < d < 100 nm		

Table 1.1: Variation of foam properties with cell diameter [4].

Structural foams

Structural foams contain a foamed inner core and a highly dense, less permeable outer layer [5]. The outer layer forms and solidifies quickly on coming into contact with mold, while the inner foam core takes time to cool and solidify, thus containing a greater number of cells than the outer layer. Commonly used structural foams in the automotive sector are modified phenylene oxide, polyoxymethylene, polystyrene, polycarbonate, polyethylene and polypropylene.

Structural foams can be produced through two methods: chemical foaming and physical foaming. Chemical foaming involves reaction and decomposition of foaming agents (70% of foam mass) to produce N_2, CO_2 and water, with the gases incorporated into the polymer to obtain the foam. In contrast, physical foaming does not require foaming agents to decompose, with the gas blown into molten polymer to obtain the foam. Chemical foaming has been used steadily over the years, while physical foaming has been frequently altered and modified, since the 1980s. While both these foaming processes are generally executed independently, they can be executed simultaneously in cases where increased foam expansion is necessary [6].

Microcellular Injection Molding

Over the past two decades, microcellular injection molding, or supercritical fluid-assisted injection molding has been considered a viable alternate to chemical foaming. This is primarily because microcellular foam parts have uniform cell diameters of 1-100 μm and cell density in range of 109-1,015 cells/cm^3 [7] . In addition, this process uses environmentally benign supercritical fluids (SCFs) such as N_2 or CO_2 as blowing agents. Thus, compared to conventionally foamed plastics, microcellular-foamed plastics have larger cell density and reduced cell size for the same reduction in weight, thereby leading to improvement in material properties.

In addition to reducing the density of molded components (and hence, their weight), microcells can also act as crack arrestors by blunting the crack tip, thereby increasing the energy requirement for crack propagation. Due to this crack-arresting feature of microcells, microcellular plastics with small cell sizes can possess high impact strength. Furthermore, SCF used in microcellular process serves as a solvent reducing polymeric viscosity. This in turn allows the processing of materials at lower temperatures, which is significant for biobased polymers sensitive to high temperatures and moisture [7].

Microcellular foaming process occurs in three steps: nucleation, cell growth and cell stabilization. In the first step, a large amount of SCF is dissolved into molten polymer at high pressure to obtain a single-phase polymer-gas solution, i.e. the polymer melt is supersaturated with the blowing agent. Following this, pressure is suddenly lowered below the saturation pressure, resulting in phase separation and thereby, cell nucleation. Finally, in the last step, nucleated cells begin to grow until they attain a cell size greater than a

critical radius value – the value below which bubbles can dissolve back into the solution[7]. Growth of cells is controlled by diffusion rate and stiffness of polymer-gas solution [7].

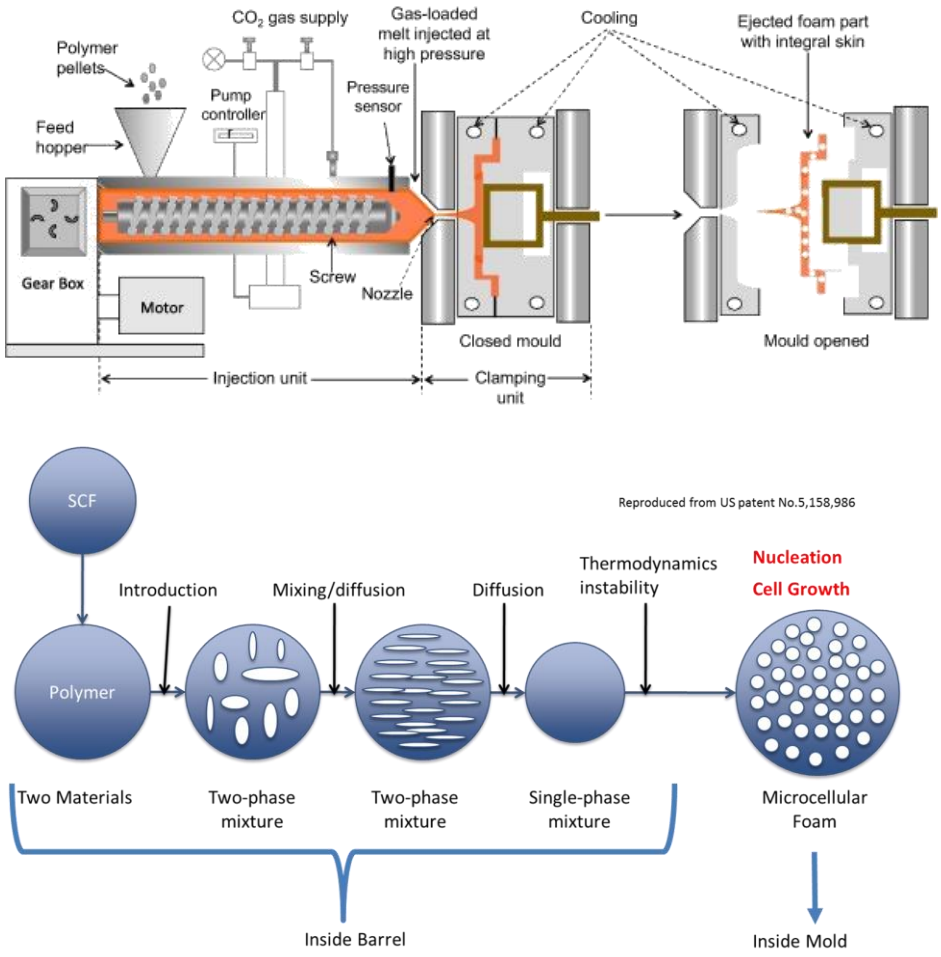

Figure 1.2: Schematic representations of supercritical fluid assisted injection molding process [8]

This thesis focuses on understanding the physical foaming behavior via SCF assisted injection molding on compatibilized and non-compatibilized PLA-PBSA systems. This thesis is divided into eight chapters. This chapter gives a detailed view on the general need for biobased thermoplastic foams in automobile sector. The second chapter explains

the state of art on current improvements with regard to improving properties of polylactic acid (PLA). The third chapter documents the materials, processing and characterization equipment used in this work. In the fourth chapter as-extruded blends are characterized via gel permeation chromatography (GPC), thermogravimetric analysis (TGA), differential scanning calorimetry (DSC) and rheometery experiments. While the fifth chapter discusses the effect of blending, addition of talc/TPP and SCF wt.% on foam microstructure. The sixth chapter details thermo-mechanical properties of solid and microcellular blends. In the seventh chapter physical and mechanical properties of the foamed and unfoamed samples are reported. Finally, the eighth chapter concludes with the findings of this thesis and documents the future outlook on microcellular injection molded plastic foams.

CHAPTER TWO

Literature Review

Biodegradable thermoplastic foams have been gaining ground in the automotive industry as they help to meet environmental regulations and standards set by the US EPA to reduce pollution through successful application of these environmentally sustainable foams. Some original equipment manufacturers (OEMs) have used biofoams to endorse bioplastics, as these foams are developed using non-biodegradable polymers (e.g. polyolefins) compounded with biodegradable materials (e.g. starch, wood flour, partially substituted cellulose, aliphatic/aromatic polyesters, or polyesteramide).

Polylactic acid (PLA) is an aliphatic polyester and potentially biodegradable polymer that has emerged as one of the most commercially successful biopolymers due to its transparency, high strength, and stiffness, making it superior to many other biobased polymers [9–12]. However, commercially available PLA has its own inherent weakness – in particular, its low toughness, heat resistance and poor processability – that prevents it from being widely adopted for durable applications. Additionally, PLA has a very slow crystallization rate, whereas high levels of crystallinity are desirable in finished products as crystallinity dictates most mechanical and thermal properties. Toughness and ductility of PLA have been improved using multiple strategies, including plasticization, copolymerization, and melt blending with different tough polymers, rubbers and thermoplastic elastomers [13–15].

Blending biopolymers with inherently toughened counterparts provides an effective medium for enhancement of their overall properties. However, most such physical blends are immiscible and might lead to deterioration in properties of PLA. Successful application of reactive compatibilization technique has provided enormous opportunities to compatibilize blends that are otherwise immiscible and incompatible. Reactive compatibilization is therefore considered to be a powerful technique with regard to effectively enhancing the compatibility of PLA with other tough polymers. Another useful way of chemical compatibilization is melt-blending of PLA with other suitable polymers, which if conducted in the presence of a reactive monomer, leads to formation of a graft copolymer at the interface, reduces interfacial tension of immiscible polymer components, and promotes interfacial adhesion. A finer phase morphology developed in blends facilitates stress transfer between the two phases, thereby improving properties of the blends.

Substantial amount of research has been carried out on physical blending and chemical compatibilization of PLA with various polymers. Jiang et al. observed toughening and improvement in melt processability of PLA upon its physical blending with poly(butylene adipate-co-terephthalate) [16]. Yamaguchi et al. found that blending PLA with poly(butylene succinate) led to improved crystallinity and enhanced processability [17]. Zhang el al. observed improvement in tensile properties of PLA upon blending with polyhydroxybutyrate [18]. Zhoa et al. reported improvements in moduli and slight decrease in tensile properties [19]. Wang et al. prepared physical and chemically compatibilized blends of PLA with poly(ε-caprolactone) through melt-blending – the latter involved the

use of triphenyl phosphite (TPP) as a coupling agent and showed improvement in elongation-at-break by 120 % compared to pure PLA[20].

Among these poly[(butylene succinate)-co-adipate] has shown the highest enhancement in mechanical and physical properties of PLA. Eslami et al. observed improvement in elongation-at-break by 250 % and strain hardening behavior for melt-blended PLA/PBSA compositions [21,22]. Ojijo et al. observed drastic improvement in impact strength (160%) upon physical and reactive blending of PLA with (PLA/PBSA) due to addition of TPP. Compatibilization through in-situ formation of compatibilizer in polymer blends has increasingly become an important alternative to the method of adding block/graft copolymers. Eslami et al. blended PLA/PBSA in presence of TPP, and observed an increase in torque values upon addition of TPP. They also observed a reduction in dispersed phase size with increase in TPP content, showing improvement in compatibility of PLA and PBSA upon addition of TPP.

On processing PLA foams, most such efforts have involved batch foaming using various blowing agents and solvents [23]. However, batch processes have limited control over various stages of foaming, and foams produced using such processes are usually meant for biomedical scaffolding applications due to their high cost and limited volume expansion. Efforts have been made in recent times to produce PLA foams using extrusion, especially to obtain high expansion ratios [24]. Research has also been pursued on producing PLA foams using microcellular injection molding over the past few years. Pilla et al. [25,26] studied the effect of addition of fillers such as multi-walled carbon nanotubes

(MWCNT), wood fiber and chain extenders on mechanical properties and foam morphology.

Bimodal cellular distribution possesses inherent advantages over their unimodal counterparts namely enhanced toughness and enhanced acoustic absorption [27]. This is because the mechanical properties are governed by both small and large cells while acoustic properties are governed by the smaller cells. However, there are nascent disadvantages these distributions pose such as decline in flexibility and complicated processing.

These distributions have been observed across different material systems processed via batch processes, extrusion processes and among few material systems with respect to supercritical foam-assisted injection molding. Most such reported bimodal distributions are the result of two blowing agents or two-step processing routes. For example, bimodal foams were observed in polycarbonate foams produced by a two-step batch process using SCF CO_2 as a blowing agent [28]. Xuetao et al. reported bimodal cellular distributions in PLA-PBAT systems reinforced with $CaCO_3$ which they attributed to foaming in amorphous and crystalline segments of PLA [29]. Extruded polystyrene foams were reported by Zhang et al. due to use of SCF CO_2 and water as co-blowing agents [30].

Few studies were found with regard to presence of bimodal cellular structure in polymers processed via SCF injection molding. Ameli et al. observed bimodal cellular distribution in PLA upon addition of talc and nanoclay as nucleating agents leading to heterogeneous nucleation [31]. Haibin et al. observed a similar structure in physically

blended PLA/PHBV in 70/30 ratio composition and attributed this to "suitable melt strength" of the blends which helped produce single polymer-gas phase [19].

Additionally, Hrishikesh et al. observed bimodality of cells in cross-linked TPU compositions. This might have been due to increase in tensile stress within the polymer matrix as a result of elongation of the polymer during cell growth, thereby facilitating the nucleation of secondary cells. Growth of secondary nucleated cells was subsequently restricted by increase in melt strength due to part cooling and depletion of SCF around the cells [32–34]. However, a fundamental understanding on bimodal distributions with respect to physical and chemically compatibilized blend morphology, addition of fillers like talc, and varying SCF gas dosages, is currently unavailable.

Hence, the objective and scope of this thesis is to study the effect of physical and chemical compatibilization of PLA/PBSA and that of addition of talc on foam microstructure. Thermal and rheological characterizations were limited to extruded blends in order to understand the effect of TPP along with determining processing conditions for injection molding. Furthermore, the effect of compatibilization in terms of obtaining unique cellular microstructures was studied, while the influence of various parameters, such as melt viscosity, SCF gas dosage, and addition of talc on obtaining the bimodal cellular distribution, was also investigated. The novelty of this work lies in understanding the effect of coupling of PLA-PBSA blends and engineering unique cellular distributions that are dependent on factors such as melt viscosity, crystallinity and branching.

CHAPTER THREE

Experimental Details

Materials:

Commercial PLA (3001 D) in pellet form was purchased from Natureworks LLC (Minnetonka, MN, USA), Its specific gravity is 1.24 and its melt flow index is around 22 g/10 min. Commercially available PBSA (Bionolle # 3001) was sourced from Showa Denko (Japan), its specific gravity being 1.23 and melt flow index being 25 g/10 min. The talc used in this study (Mistrocell M90) was supplied by Imerys Talc with mean diameter of 18.8 μm. The coupling agent triphenyl phosphite (TPP) was obtained from Sigma-Aldrich. N_2 with purity levels of 99.9 % was used as the physical blowing agent in microcellular injection molding.

Sample	Nomenclature	PLA	PBSA	Talc	TPP (Coupling Agent)
Pure PLA	A	100	-	-	-
Pure PBSA	B	-	100	-	-
Physical Blend	P	70	30	-	-
Compatibilized blend	C	70	30	-	2
Physical Blend + Talc	PT	70	30	5	-
Compatibilized blend +Talc	CT	70	30	5	2
PLA + Talc	AT	95	-	5	-
PBSA + Talc	BT	-	95	5	-

Table 3.1: Design of Experiment (DOE) formulations for this study (weight %)

Processing:

Prior to processing, all materials were vacuum dried overnight. The selected compositions (presented in Table 3.1) were melt blended using a co-rotational twin screw extruder (ZSK 30 from Werner & Pfleiderer). Extrusion conditions have been listed in Table 3.2. Eight compositions were prepared for this work.

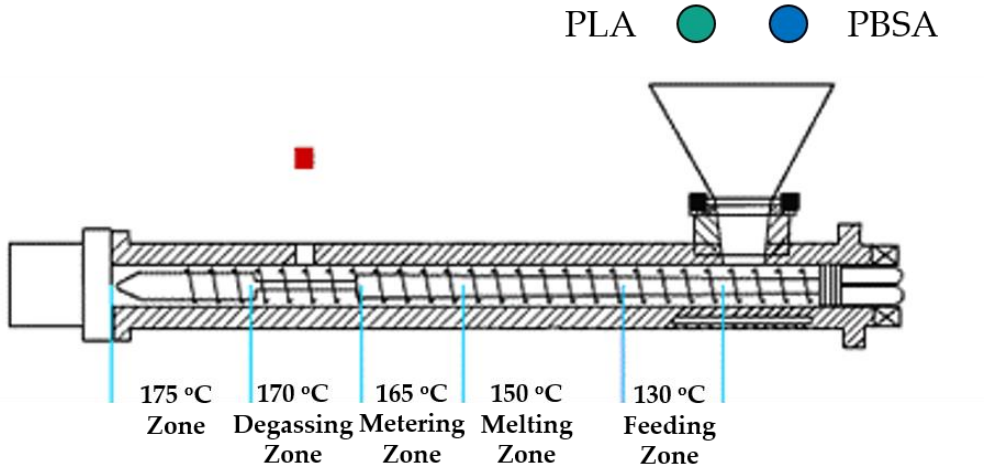

Figure 3.1: Schematic representation of the extruder with heating zones [35]

Parameter	Value
Drying temperature (°C)	75
Drying time (h)	8
Screw rotation speed (rpm)	35
Barrel temperatures (°C)	175,170,165,150,130

Table 3.2: Experimental conditions for melt blending PLA-PBSA compositions

Parameter	Solid Molding	Foamed Molding
Drying temperature (°C)	80	80
Drying time (h)	8	8
Back pressure (MPa)	10	80
Melt temperatures (°C)	155/165/175/185/195	155/165/175/185/195
Injection pressure (bar)	2500	2500
Injection speed (cm^3/s)	65	65
Holding pressure (bar)	800	0
Holding time (s)	3	0
Cooling time (s)	60	60
Screw rotation speed (rpm)	127	127
Mold temperature (°C)	24	24
Gas dosage (wt%)	0	0.73 and 0.94
Shot volume (cm^3)	21.5	19

Table 3.3: Experimental conditions for solid and microcellular injection molding

Microcellular injection molding was carried out using an Arburg Allrounder 3205 equipped with a Trexel Series II SCF dosing system (Table 3.3). Supercritical N_2 was used and its weight % was determined by the initial SCF delivery pressure at the beginning of the dosing process, melt pressure inside the barrel during dosing and the duration for which the SCF injector remains open with respect to the injection shot volume. Temperatures were reduced for pure PBSA to 100/140/145/135/125 ^oC. In the metering zone temperatures had to be increased to ensure consistent pressure drop during gas dosage. Twenty-four compositions each consisting of 10 samples were prepared.

As-extruded pellets were characterized using gel permeation chromatography (GPC), Thermogravimetric analysis (TGA), differential scanning calorimetry (DSC), and

rheometry. GPC was performed to understand the effect of physical and reactive extrusion for all blends. The thermal stability and crystallinity of these pellets were studied using TGA and DSC via physical and compatibilization of PBSA and addition of talc. Rheological tests were carried out to study the effect of physical and compatibilized PBSA and addition talc. However, the injection molded samples were characterized via SEM, tensile tests and DMA in order to understand the effect physical and chemical compatibilization of PLA-PBSA on foamed microstructure, mechanical and thermo-mechanical properties to establish structure property relationship.

Gel Permeation Chromatography:

The number average molecular weight (M_n) and polydispersity index (PDI) for all samples after extrusion, were determined by gel permeation chromatography (GPC) on a Waters GPC equipped with a UV/Vis and RI detector. Chloroform was used as an effluent (flow rate 1.0 mL/min) at 33 ºC. All samples were prepared as 0.5 % (weight/volume) solutions in chloroform, with approximately 50 µL of sample injected into GPC. Prior to injection, the dissolved solution was filtered using a 0.2 µm PTFE filter. Calibration was done using narrow molecular weight PS standards ranging from 990500 to 436.

Thermo-gravimetric analysis:

Thermo-gravimetric analysis (TGA) was performed on a TA Thermogravimetric Analyzer Q5000. All specimen weighed between 20-30 mg and were heated from room temperature to 550 °C at 10 °C/min under nitrogen atmosphere.

Differential scanning calorimetry:

Differential scanning calorimeter (TA Instruments, Q2000) was used to study the crystallization behavior of pure and blended polymers. About 7-9 mg weight of different specimen were taken in hermetically sealed aluminum pans. The specimens were subjected to heating/cooling/heating cycles at 5 °C/min. The samples were first heated from 25 °C to 250 °C (to remove any thermal history from processing), held isothermally for 5 min and cooled to 25 °C, and subsequently ramped to 200 °C. Crystallization temperature (T_c), melting temperature (T_m), apparent melting enthalpy (ΔH_m), and enthalpy of cold crystallization (ΔH_{cc}) were determined using these DSC curves. Crystallinity of PLA and PBSA was calculated by the relation:

Equation 3.1:

$$\chi_c\,(\%\,crystallinity) = \frac{\Delta H_m - \Delta H_{cc}}{\Delta H^0} \times \frac{100}{W}$$

Where ΔH^0(PLA) and ΔH^0(PBSA) are the enthalpies of melting per gram of 100 % crystal (perfect crystal) of PLA and PBSA (93.7 and 142 J/g) respectively, and W is the weight fraction of PLA and PBSA in the blend [36].

Scanning Electron Microscopy (SEM):

Morphology of solid and microcellular injection molded specimen were studied using a scanning electron microscope (Hitachi S-4800) at an accelerating voltage of 5.0 kV. Specimen were taken from the cross-section of gauge length of tensile specimen. The specimens were cryogenically fractured by introducing a notch prior to exposure to liquid nitrogen. Surfaces of these specimen were then sputter-coated with platinum using a

Hummer 6.2 Sputtering System. Cell size was analyzed using an image analysis tool (Image J) and cell density was calculated using the relation:

Equation 3.2:

$$\text{Cell density} = \left(\frac{N}{L^2}\right)^{\frac{3}{2}} M$$

Where N is the number of cells, L is the linear length of area, and M is a unit conversion, resulting in cell density being expressed as the number of cells per cubic centimeter. In order to avoid skewing of data, a few abnormally large voids that were observed in some specimen were excluded from the calculation of average cell size and cell density.

Rheological Measurements:

Rheological measurements were performed using a capillary rheometer system model 3211 from Instron. The diameter and L/D ratio of the capillary die in rheological measurements were 0.93 mm and 33. The pellets were fed into the rheometer barrel which was heated to 190 ^{o}C in order to study the melt viscosity of the samples.

Tensile:

Tensile tests were performed on Type I specimen in accordance with ASTM D638 using an Instron (5967) universal testing machine. The specimen was positioned between static movable clamps with a crosshead speed of 5 mm/min. Five samples were tested for each composition.

Dynamic Mechanical Analyzer

Dynamic mechanical analysis was carried out using a TA Q800 Dynamic Mechanical Analyzer. Rectangular specimens with dimensions of 4 x 8 x 70 mm were cut from the gauge length of injection-molded specimen and tested in dual cantilever mode. Samples were tested at temperatures between -70 to 100 °C at a heating rate of 3 °C/min with a 1 Hz frequency and a 0.1 % strain amplitude in order to determine glass transition temperature, storage and loss modulus.

Relative Density

Relative densities of samples were measured by comparing tensile specimens of similar shot volume made from Polystyrene. In this thesis all samples were compared to polystyrene tensile specimen of known mass and density and documented in the appendix.

CHAPTER FOUR

Characterization of as-extruded Blends and Composites

Several researchers have studied the reaction between TPP and polyester, leading to development of two reaction mechanisms – one by Jacues et al. [37] and the other by Aharoni et al. [38]. In both mechanisms, the first step is preferential reaction of hydroxyl end groups with TPP by displacing one of TPP's phenoxy groups in Scheme 4.1. This leads to the formation of an intermediate phosphorus-containing compound. The second step depends upon the reaction mechanism. The first mechanism involves the phosphorus atom from TPP becoming a part of the extended polymeric chain. Since TPP contains three phenoxy groups, a multi-substitution process can occur, followed by phenol elimination displacing the intermediate product-related equilibrium (as shown in Scheme 4.2). Till phosphorus atoms eventually become a part of the extended polymeric chain, this substitution is believed to continue.

Conversely, the second mechanism observes the occurrence of ester linkages from polymers. Instead of the hydroxyl end groups, it is carboxyl groups that react with the phenoxy groups of intermediate product (diphenyl phosphite) obtained after the first step, resulting in chain extension without the phosphorus atom becoming part of the extended polymeric chain (Scheme 4.3).

For all the reaction schemes mentioned, chain extension and/or interchange is observed.

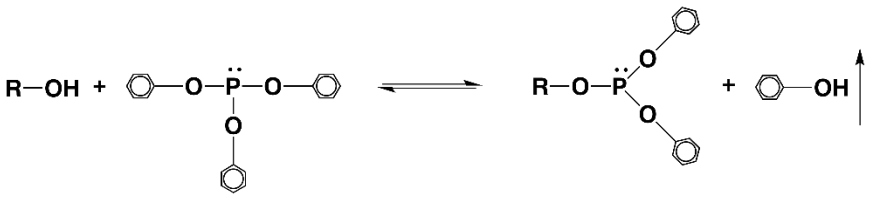

End group of PLA/PBSA + TPP → Reacted polymeric chain + Phenol

Scheme 4.1: Initiation of reaction between TPP and PLA/PBSA

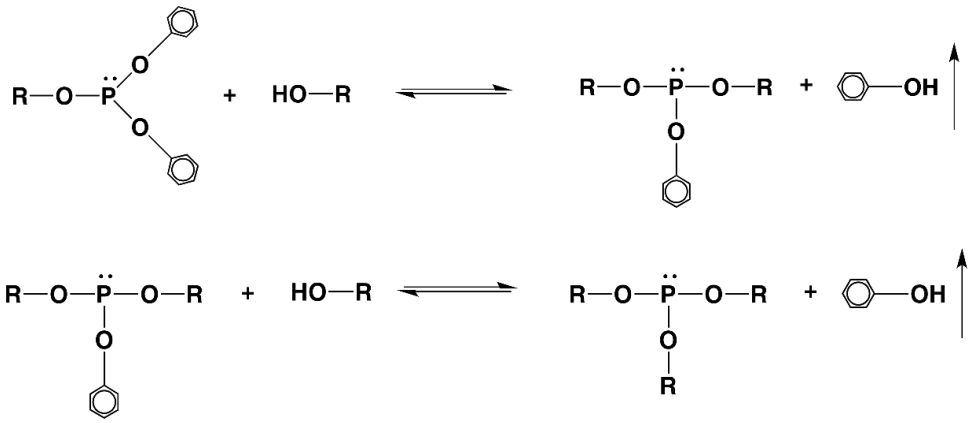

Scheme 4.2: Propagation reaction inducing possible branching mechanism between hydroxyl chain ends of PLA/PBSA polymeric chains

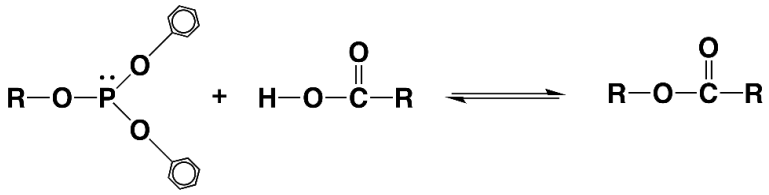

Scheme 4.3: Propagation reaction inducing possible chain extension mechanism between hydroxyl chain ends of PLA/PBSA polymeric chains

Sample	M_n	PDI	Area (cm^2)
PLA	102,862	1.8	26625
PBSA	67,671	2.0	75660
PLA+PBSA	83,014	1.9	34000
PLA+PBSA+TPP	108,598	1.4	17793

Table 4.1: M_n, M_w, PDI and area for non-talc samples after extrusion

M_n, M_w, PDI and area were measured for all solid samples and tabulated in Table 4.1 and 4.2. As can be observed from Table 4.1 number average molecular weight of the physical blends was found to be between the M_n for PLA and PBSA. The compatibilized blends showed an increase in M_n and a decrease in PDI indicating a narrow molecular weight distribution. The decrease in area for PLA-PBSA-TPP might suggest that crosslinking or branching might occur.

Addition of talc marginally decreased the molecular weight of most samples except PLA and a similar decline in area was also observed. In order to better explain these results the exact mechanism of chain extension and chain interchange reactions, as promoted by TPP, should be understood.

Sample	M_n	PDI	Area(cm^2)
PLA + Talc	79,750	2.215	31365
PBSA + Talc	65,553	2.133	60649
PLA+PBSA+ Talc	83,676	1.805	35834
PLA+PBSA+TPP+Talc	113,555	1.438	15622

Table 4.2: M_n, M_w, PDI and area for talc samples after extrusion

In case of multiple reactions, the phosphorus molecule becomes a binding point between different polymer chains. Thus, a molecular weight increase and finally branching can occur, this has been observed in a study conducted by Jacues et al. wherein TPP was used to melt blend PET/PBT [37].

Thermal Characterization

Thermal degradation of PLA, PBSA and PLA/PBSA blends was investigated via thermo-gravimetric analysis (TGA) in air at 10 °C/min. Figure 4.1(a) shows PLA having higher thermal stability than PBSA. Additionally, the compatibilized blends showed a decrease of 5 and 10 % weight loss (T_5 and T_{10} values) by 5 °C with respect to pure physical PLA/PBSA blend, indicating branching might have occurred during melt blending with TPP. This is due to the fact that branching reduce crystallinity thereby leading to decreased thermal stability [39]. Addition of 5% talc was observed to lead to marginal increase the thermal stability of all compositions along with increase in total residual content by ~ 5% (Figure 4.1-(b)).

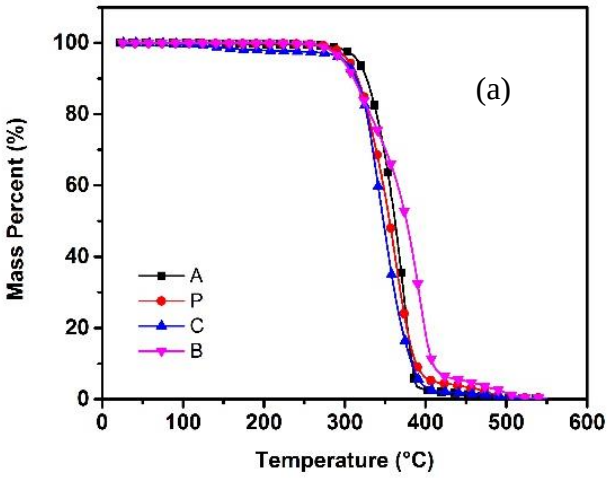

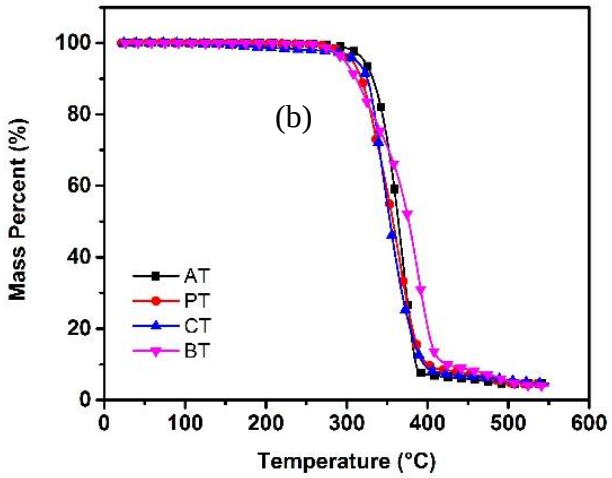

Figure 4.1: TGA curves of (a) Non-Talc and (b) Talc Compositions

DTG of PLA/PBSA blends shown in

Figure 4.2-(a) exhibited a maximum degradation temperature of ~ 371 °C for PLA (A) and 393 °C for PBSA (B). Physical PLA/PBSA (P) blends showed a similar DTG between PLA and PBSA, while the compatibilized blends showed significant shift in DTG – nearly 20 °C lower than PLA/PBSA blends – further reinforcing the possibility of branching occurring. Furthermore, PLA/PBSA (P) showed prominent shoulder at 336 similar to the one shown by PBSA, while PLA-PBSA-TPP (C) blend showed no shoulder.

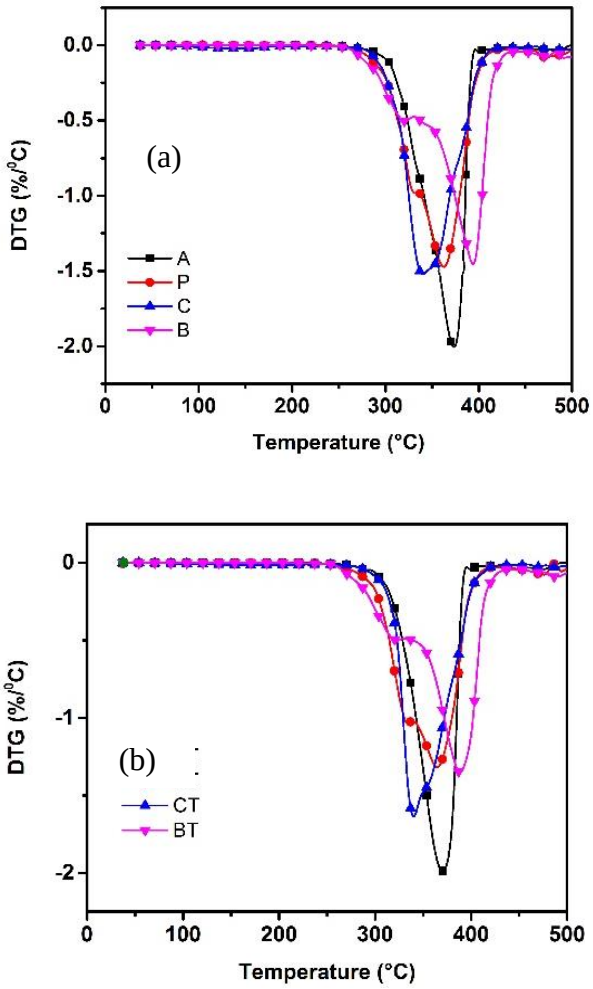

Figure 4.2: DTG curves of (a) Non- Talc and (b) Talc Compositions

Sample	T_5 (˚C)	T_{10} (˚C)	DTG (°C)	Residue %
A	315.8	326.9	371.2	0.12
B	297.6	311.2	393.2	0.38
P	304.6	316.0	355.6	0.41
C	299.4	314.1	338.2	0.21
AT	321.5	332.1	370.1	4.62
BT	297.2	311.5	341.1	4.64
PT	306.9	318.0	361.2	4.64
CT	301.9	315.4	339.5	4.63

Table 4.3: Summary of the T_5, T_{10}, DTG and residue % for PLA, PBSA, PLA-PBSA, PLA-PBSA-TPP with and without the addition of talc

Differential scanning calorimeter curves shown in

Figure 4. were obtained during their second heating run. The curves revealed glass transition for all PLA and PLA-based blends, cold crystallization for non-talc blends, and melting peaks (Tm_1 for all non-talc samples and Tm_2 for all talc-blended samples).

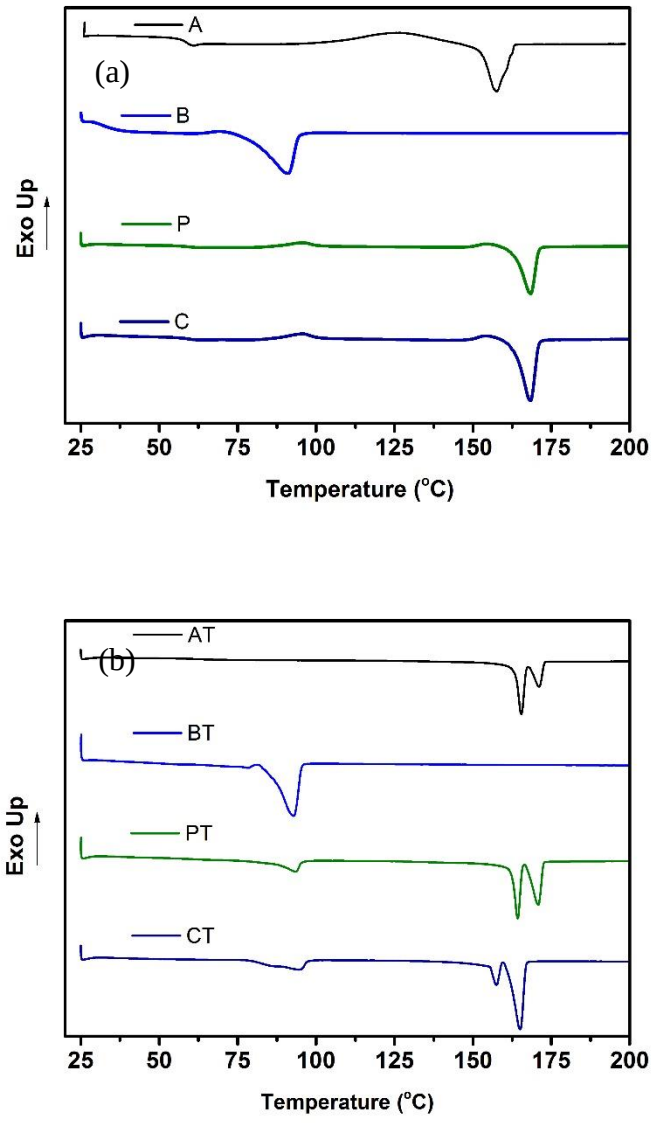

Figure 4.3: DSC curves of the second heating cycle at 5 °C/min

Sample	T_g°C	T_{cc}°C	Δ H_{cc} (J/g)	T_{m1}°C	T_{m2}°C	Δ H_m (J/g)	% Crystallinity
A	60.1	133.7	18.2	162.7	-	25.2	7.7
B	-	-	-	91.0	-	44.3	-
P	58.6	95.8	4.7	168.3	-	32.0	29.1
C	55.6	95.4	4.6	163.2	-	28.8	25.1
AT	60.8	-	-	165.4	171.2	31.5	35.3
BT	-	-	-	92.9	35.8	34.9	-
PT	-	-	-	164.3	167.3	28.4	45.6
CT	-	-	-	157.6	165.0	27.1	43.5

Table 4.4: Thermal Properties of as extruded blends obtained from DSC

T_g of pure PLA (A) was observed to be approximately 60 °C, while that of PBSA was observed to be below room temperature (~ -45 °C). Physical PLA/PBSA blends (P) showed a drop in T_g to 58.60 °C while compatibilized blends showed a higher drop in T_g to 55.69 °C. This could be attributed to two factors: (i) compatibilization of PLA and PBSA, making the two polymers partially miscible at the interface and thereby, pushing T_g of PLA towards that of PBSA, and (ii) plasticization effect of TPP and phenol, due to compatibilization reactions. It has been shown that compounds such as triphenyl phosphate (TPP) can act as plasticizer of PLA [40]. Plasticizers typically weaken intermolecular forces between polymer chains, thereby causing reduction in T_g. Presence of talc did not impact T_g of PLA (A) in any significant measure, as has been reported in several prior studies [41,42].

Single melting peaks (T_{m1}) for PLA (A), PBSA (B), PLA-PBSA (P) and PLA-PBSA-TPP (C) were observed, with PLA (A) showing melting at 162 °C, PBSA at 92 °C and the blends showing an increase in melting point to 168 °C. Addition of talc led to bimodal melting peaks attributed to heterogeneous nucleation effect of talc particles,

resulting in two types of crystal structure [43]. The melting temperatures showed behavior similar to non-talc compositions. Crystallinity of pure PLA (7.7%) increased with physical (29%) and chemical (25%) compatibilization with PBSA. This could be attributed to reduction in viscosity in both blends, as confirmed by rheology tests, can accelerate the formation of hard crystalline segments [44]. Additionally, addition of TPP led to formation of branching as shown in earlier leading to a lesser crystallinity when compared to the physical blends.

Rheological Characterization

Melt strength of the polymer is another parameter that is vital to processing and foamability vis-a-vis SCF assisted injection molding. Melt strength is related to molecular chain entanglements of the polymer and its resistance to untangling under strain. While extensional viscosity is usually a good measure of melt strength, it is linearly related to shear viscosity by the Trouton's ratio, thereby relating melt strength to shear viscosity [45]. The shear viscosity of the as extruded pellets were studied at temperatures of 190^{o}C in order to better understand and explain the relationship between melt viscosity and microstructure of these foams.

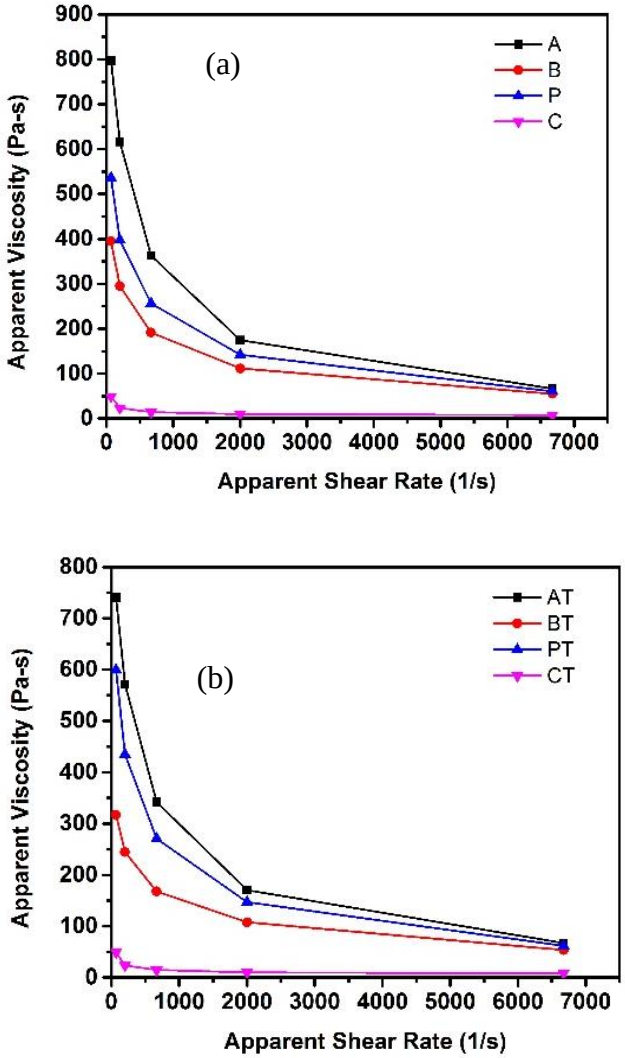

Figure 4.4: Apparent Viscosity Vs Shear Rate for (a) Non-Talc and (b) Talc compositions

As seen in Figure 4.4- (a), apparent viscosity of PLA was substantially higher than that of PBSA. Physical PLA/PBSA blends resulted in lowering of apparent viscosity, while addition of TPP had a dramatic plasticization effect on these blends, as observed in several studies [46,47]. Additionally, compatibilizers have been known to plasticize blended systems and lower the melt viscosity [48]. Another reason for the drop in melt viscosity

could be attributed to the release of phenol during reactive extrusion which might be contributing to the lubricating effect.

CHAPTER FIVE

Effect of Process Parameters on Cellular Morphology

Cellular morphology of microcellular injection-molded PLA, PBSA and PLA/PBSA blends was found to vary with SCF gas dosage, content of talc added, and compatibilization between PLA and PBSA Figure 5.1 and Figure 5.2 shows SEM micrographs of cryogenically fractured non-talc and talc samples respectively. 3 samples in each composition were fractured and analyzed along their respective cross-sections. Micrographs of solid samples have also been shown for comparison in Figure 5.1 and Figure 5.3. Cryogenically fractured solid PLA (Figure 5.1 -as) showed relatively smooth, mirror-like fracture surface as has been observed in earlier studies [49]. With respect to foaming, solubility of supercritical N_2 in PLA is ~ 2 % in the temperature range of 180 - 210 $^{\circ}$C while also showing high diffusivity [50]. Supercritical foaming of PLA resulted in uniformly distributed spherical cells as shown in Figure 5.1-a1 and a2.Figure 5.**1**-a1 and a2 indicates foaming of PLA at different SCF wt. %, resulting in lowering of cell sizes (52 and 41 μm) and increase in cell density from 1.5 x 10^6 to 1.12 x 10^7 cells/ mm^2, as summarized in Figure 5.5. Figure 5.**1**-bs shows solid PBSA fractogram exhibiting dimples on the surface morphology, a feature inherently observed in ductile polymers. Foamed PBSA showed non-uniform cell structure (Figure 5.1-b1 and b2) which might be due to its elastomeric nature making it difficult for uniform foaming to occur [44]. PBSA showed relatively larger cell sizes of 80 and 70 μm with respect to both SCF gas dosages, resulting in cell density of 5.6–7.7 x 10^6 cells/mm^2, as summarized in Figure 5.5.

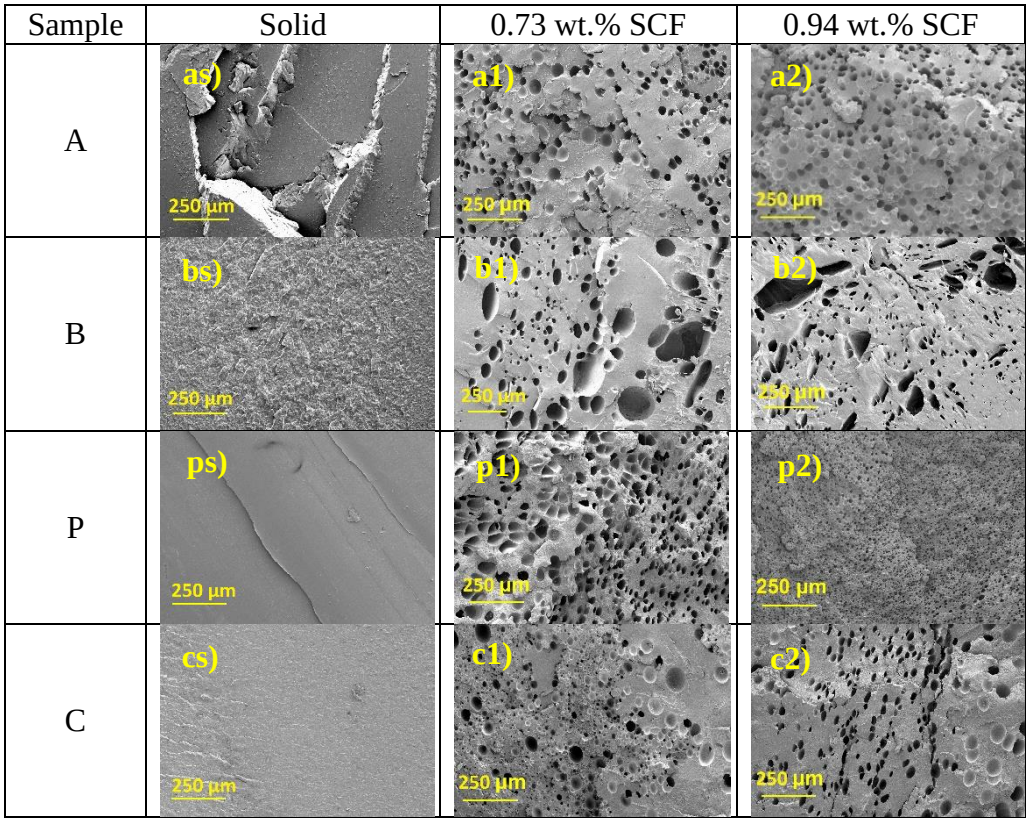

Figure 5.1: SEM Micrographs of PLA (A), PBSA (B), PLA-PBSA (P) and PLA-PBSA-TPP (C) obtained via cryogenic fracture

Physical blending and compatibilization of PLA and PBSA revealed differences in surface morphology at higher magnification. Physical blends showed brighter fibrils in a darker matrix, indicating possible phase separation of PBSA from PLA, while the compatibilized blends showed co-continuous morphology, as seen in Figure 5.3 and reported by Ojijo et al. [21]

Sample	Solid	0.73 wt.% SCF	0.94 wt.% SCF

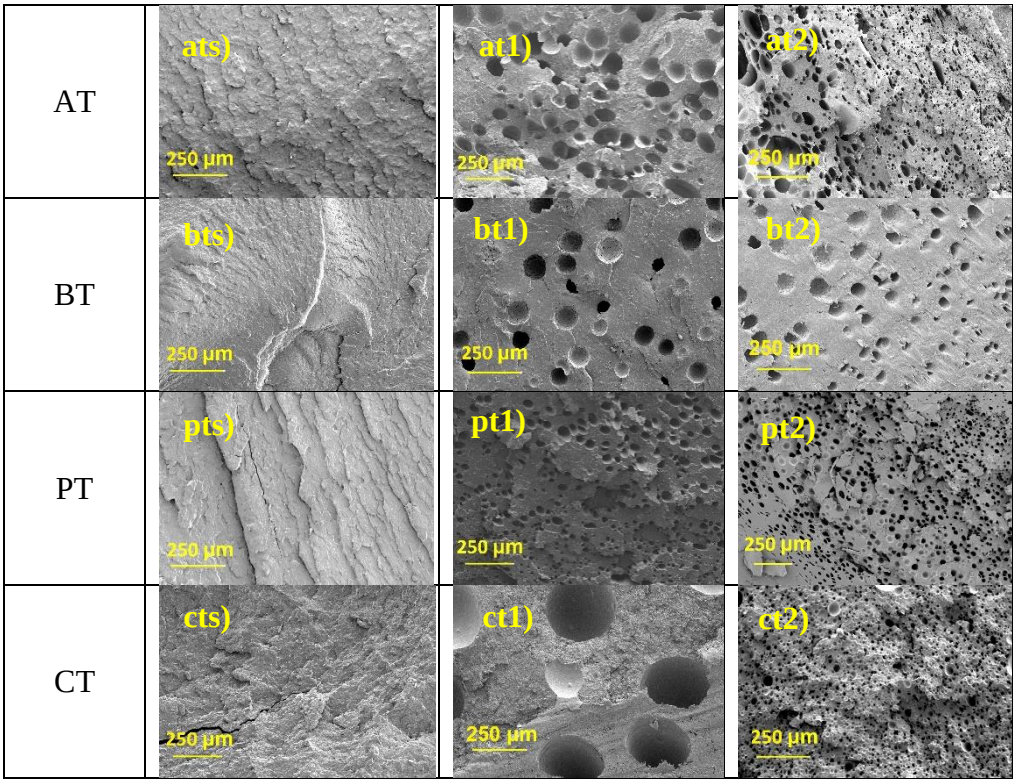

Figure 5.2: SEM Micrographs of talc filled microcellular injection molded PLA (AT), PBSA (BT), PLA-PBSA (PT) and PLA-PBSA-TPP (CT)

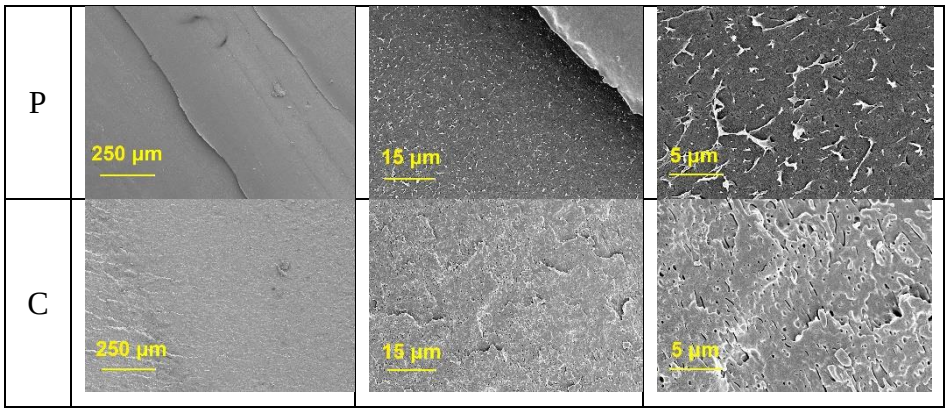

Figure 5.3: SEM images of solid PLA/PBSA and PLA/PBSA/TPP showing change in surface morphology

Physical blends, as shown in Figure 5.1-p1 and p2, exhibited varying cell sizes (43 and 18 μm) and cell density (ranging from 6 x 10^6 cells/mm^2 to 4.3 x 10^7 cells/mm^2). This significant increase in cell density can be attributed to nucleation of cells at the interphase between the two polymers and inherently unique foaming of individual polymers and in the interface of these polymers, as observed for both PLA and PHBV foams [19]. However, compatibilization had a significant effect on foaming and resulted in bimodal cellular structure (Figure 5.4) wherein two distinct cell sizes were observed: the smaller cell size was 5% - 50% of the average of larger cell sizes as shown in Figure 5.5 Additionally, foaming in the branched region might vary from the foaming observed in individual polymer or their physical blends. Histograms for all samples are presented in Appendix B.

In contrast, physical blends did not demonstrate bimodality which could be due to two reasons: higher melt strength, leading to a more uniform cell growth; and the presence of several nucleation sites at the interface of the blends, which in turn disrupted segregated foaming within these polymers.

With respect to all pure compositions, higher gas dosage resulted in smaller cell size and higher cell density, while lower gas dosage may have resulted in cell coalescence, resulting in larger cells (Figure 5.1-a1 and b1). This could be attributed to the higher supercritical fluid/polymer ratio, permitting the nucleation of a larger amount of cells per cubic centimeter [51].

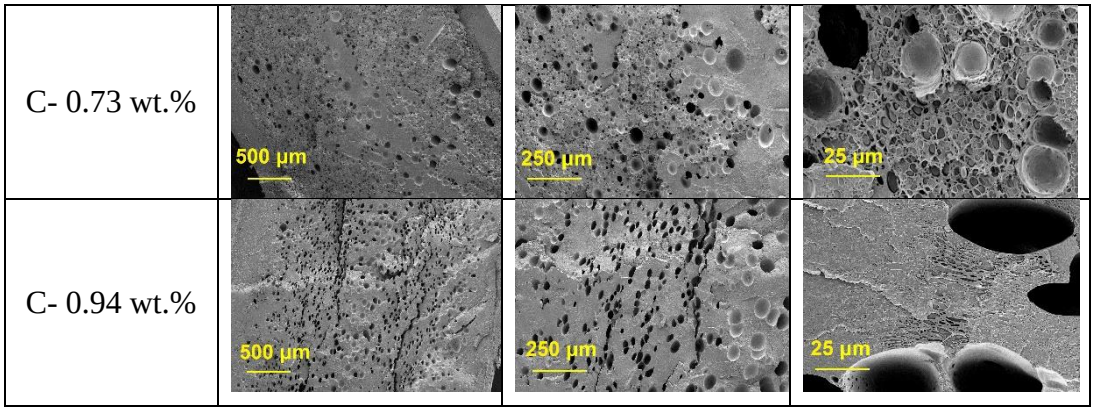

Figure 5.4: SEM images of bimodal cellular distributions of PLA/PBSA/TPP at 0.73 and 0.94 wt% SCF gas dosage

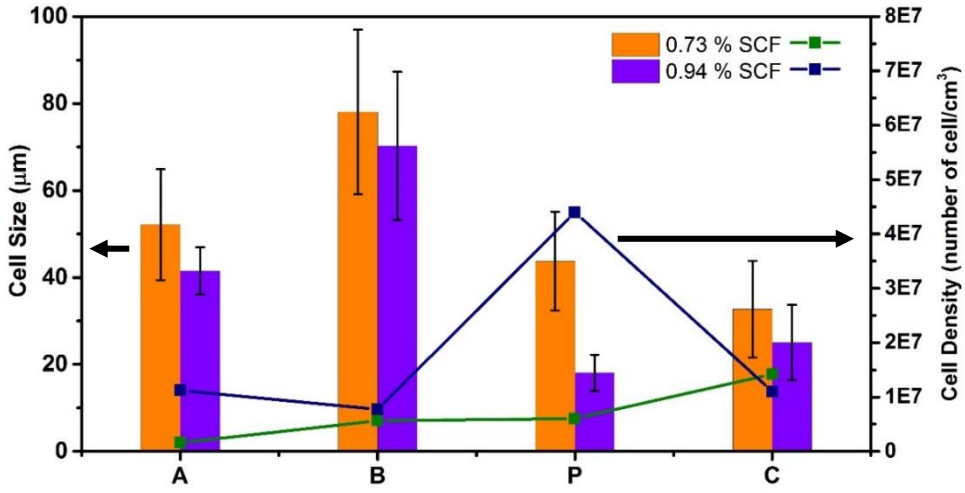

Figure 5.5: Cell size and cell density of microcellular injection molded PLA (A), PBSA (B), PLA-PBSA (P) and PLA-PBSA-TPP (C)

Effect of Talc

Addition of talc effects cellular morphology as talc particles act as heterogeneous nucleation sites due to their small size and large surface area. This provides a large number of cell nucleation sites, resulting in larger cell density and smaller cell size while reducing the energy barrier for nucleation, thereby increasing nucleation density [52–54]. As seen in Figure 5.2-at1 and at2, foaming of PLA at lower SCF dosages resulted in large spherical

cells of sizes 47 and 33 μm with lower cell densities of 7.3x 10^6 cells/mm^2. However, at higher SCF dosage of 0.94 %, PLA foams resulted in fine cellular morphology with a cell density of 1.5 x 10^7 cells/mm^2.

Addition of talc to PBSA led to obtainment of uniform spherical cells with cell size of 90 and 43 μm .

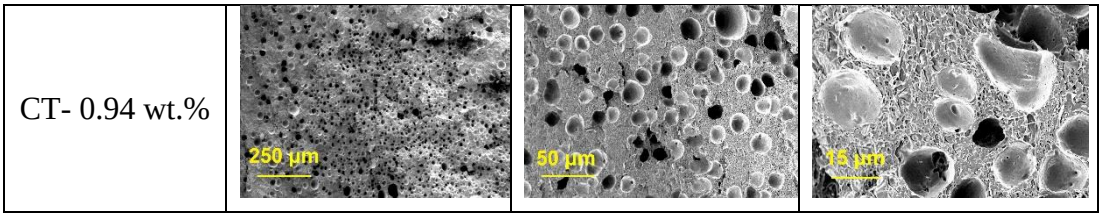

Figure 5.6: SEM images of bimodal cellular distributions of PLA/PBSA/TPP/Talc (CT) at 0.94wt% SCF gas dosage

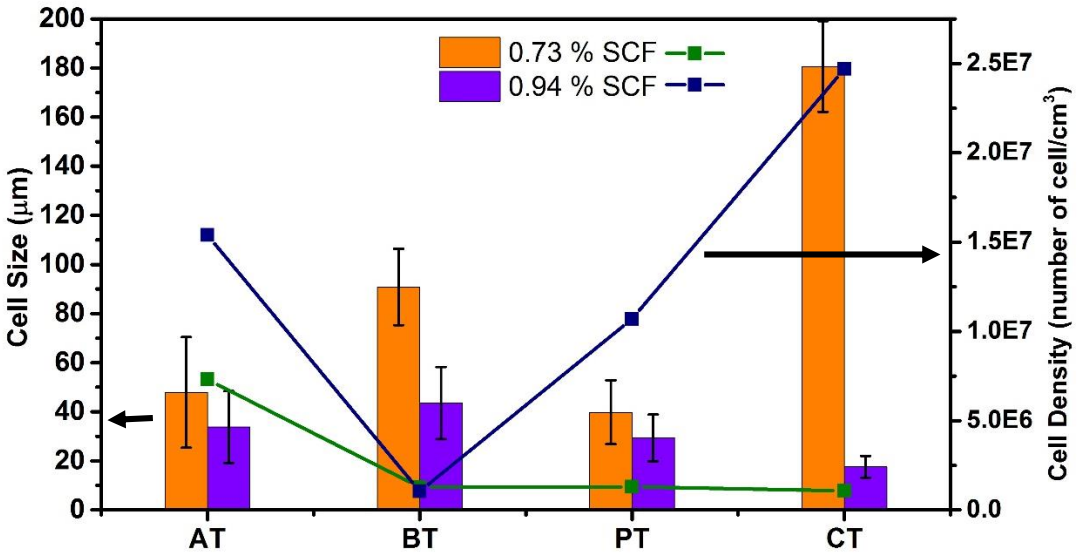

Figure 5.7: Cell size and cell density of talc filled microcellular injection molded PLA (AT), PBSA (BT), PLA-PBSA (PT) and PLA-PBSA-TPP (CT)

Talc-based physical blends resulted in smaller cell sizes compared to PLA/PBSA blends along with a uniform cell morphology at both SCF gas dosages and reduction in

average cell size (40 to 30 μm) and increase in cell density (1.28 x 10^6 cells/mm^2 to 1.07 x 10^7 cells/mm^2) as seen in Figure 5.7. The compatibilized blends as shown in

Figure 5.**2**-ct1 and ct2 exhibited unusually large cell sizes of 190 μm at a lower gas dosage of 0.74 wt. %, which reduced drastically to 17 μm for SCF dosage of 0.94 wt. %. This might be due to improper dissolution of SCF gas in the polymer melt. Furthermore, bimodal distribution was observed in the compatibilized blend at SCF dosage of 0.94 wt. % (Figure 5.6). In summary, addition of talc was observed to lead to reduction in cell size and increase in cell density in most cases with regard to PLA, PBSA and PLA/PBSA blended foams.

Sample	Core Length (mm)		Skin Thickness (mm)		CDI	
	0.73 wt%	0.94 wt%	0.73 wt%	0.94 wt %	0.73 wt%	0.94 wt %
A	2.7	2.6	0.4	0.5	1.0	1.0
B	3	2.9	0.1	0.3	1.0	1.2
P	2.7	2.7	0.5	0.4	1.0	1.0
C	2.4	2.5	0.6	0.5	1.2	1.2
AT	2.8	2.9	0.6	0.6	1.0	1.1
BT	2.4	2.4	0.6	0.6	1.0	1.2
PT	2.6	2.7	0.6	0.5	1.1	1.1
CT	2.1	1.5	1.0	1.9	1.0	1.2

Table 5.1: Summary of Core/Skin thickness and CDI for all specimens

Cellular distribution from SEM micrographs can also be used to quantitatively determine polydispersity, more commonly referred to as Cell distribution Index (CDI) [55]. In general, CDI indicates the extent of uniformity in cell size – a value of close to 1 for CDI value reflects uniform cell size. CDI values [56] for PBSA (B) and PBSA-Talc (BT)

showed an increase from their counterparts due to non-uniform foaming, as has been explained earlier.

Among the blends which exhibited bimodal cellular morphology, such as PLA-PBSA-TPP (C) and PLA-PBSA-TPP-Talc, a higher value of CDI (1.2) was observed due to the presence of bimodal distribution. Microcellular injection-molded parts have a foamed core region and two un-foamed skin layers (Figure 5.8) on the cross-sectional fractured surface, primarily due to rapid cooling of polymer melt that comes in contact with the metal mold, leading to an un-foamed skin [57].

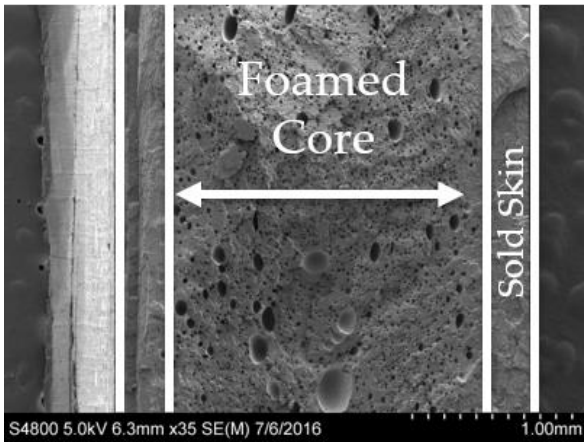

Figure 5.8: Representation of skin and core thickness observed under an SEM

SEM micrographs were analyzed to determine the core and skin thickness in an effort to understand the SCF foaming in pure and blended samples. Pure PLA (A) samples showed foamed core thickness of 2.6-2.7 mm and skin thickness of 0.44-0.50 mm. Pure PBSA showed larger foamed cross-section, primarily due to non-homogenous nature of these foams. Physical blends had a larger foamed core in comparison to the compatibilized blends, which could be due to foaming at the interface of the two polymers.

With respect to the radius of nucleating cells, the rate of change of cell radius, R, is controlled by melt viscosity η, gas pressure in micro-cell P_g, surface tension at the interface of the melt and the gas (σ) and melt pressure at the outer boundary of the cell P [7].

Equation 5.1: Relation between melt viscosity and rate of change of critical radius

$$\frac{dR}{dt} = \frac{1}{\eta}[(P_g - P)R - 2\sigma]$$

PBSA blends resulted in lowering of apparent viscosity, while addition of TPP had a dramatic plasticization effect on these blends, as observed in several studies [46,47]. Also, compatibilizers have been known to plasticize blended systems and lower melt viscosity [48].

CHAPTER SIX

Thermomechanical Properties

The viscoelastic properties of solid and microcellular PLA, PBSA, PLA-PBSA, PLA-PBSA-TPP with and without talc were studied using DMA to track the temperature dependence of the storage modulus, loss modulus and tan delta.

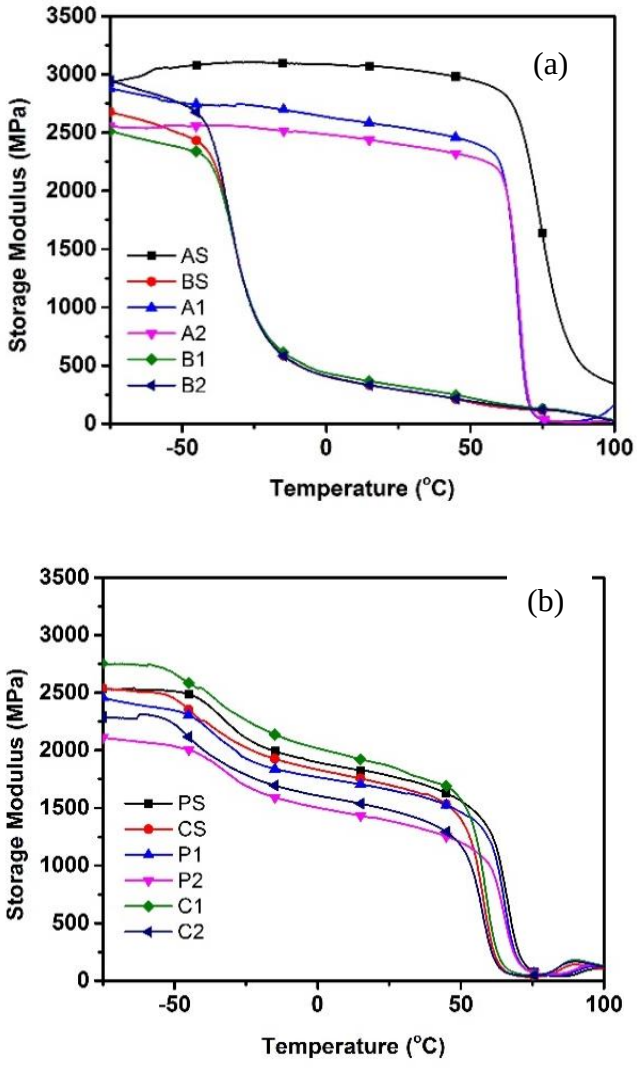

Figure 6.1: Storage modulus of non-talc (a) pure (b) blends compositions

From Figure 6.1, it is observed that the storage modulus for all solid and microcellular samples declined with increasing temperature Figure 6.2 shows solid and microcellular samples of PLA (AS, A1 and A2) rapidly reducing at 63 ^{o}C around the glass transition temperature. Figure 6.1 also shows PBSA (BS, B1 and B2) experiencing a sharp decline indicating its glass transition below 0 ^{o}C Both SCF gas dosages led to lower storage moduli in the case of PLA and PBSA.

The solid and foamed physical blends (PS, P1 and P2) exhibited a glass transition at 62 ^{o}C while the compatibilized blends (CS, C1 and C2) T_g was shifted to 53 ^{o}C indicating some effective plasticization of PLA-PBSA by TPP.

Overall PLA showed a higher storage modulus compared to PBSA and the blends, indicating that addition of PBSA had a strong influence over the elastic properties especially in the low temperature regime.

The solid physical and compatibilized blends showed distinct storage moduli of 2600 MPa below 0 ^{o}C. Microcellular samples of PLA-PBSA (P1 and P2) exhibited a lower storage moduli (2454 and 2107 MPa) which could be attribute to the smaller cells and higher cell densities exhibited by them, this behavior was also exhibited by microcellular PLA-PHBV samples [19].

Interestingly the foamed compatibilized blend at the lower SCF gas dosage (C1) exhibited storage modulus higher than its solid counterpart's due to the bimodal cellular distribution. The microcellular sample with the lower SCF gas dosage (C1) had a storage modulus higher than its physically foamed counterpart (P1 and P2) and its own solid counterpart (CS).

For samples with talc a similar trend of decreasing storage modulus vs. temperature was observed was observed. Figure 6.2 shows a rapid decline in the modulus for all PLA-Talc and PBSA –Talc samples at 60 ^{o}C and -43 ^{o}C close to their glass transition found in via DSC. The solid and physically foamed blends (PTS, PT1, PT2) showed a glass transition at 65 ^{o}C, while the compatibilized blends (CS, C1 and C2) T_g was shifted to 53 ^{o}C indicating some effective plasticization of PLA-PBSA by TPP.

Overall all talc based samples exhibited a higher storage modulus compared to their non-talc counterparts. This could be attributed to the fact that talc has a moduli at least one order of magnitude higher than most polymers, which might allow for an effective stress transfer from the matrix to the talc filler, leading to higher load-bearing capabilities [58,59].

The solid non-compatibilized and compatibilized talc filled samples showed very interesting results below 0 ^{o}C. Solid samples of PLA-PBSA-Talc (PTS) showed a higher storage modulus of 2931 MPa compared to their compatibilized PLA-PBSA-TPP-Talc (CTS) counterparts.

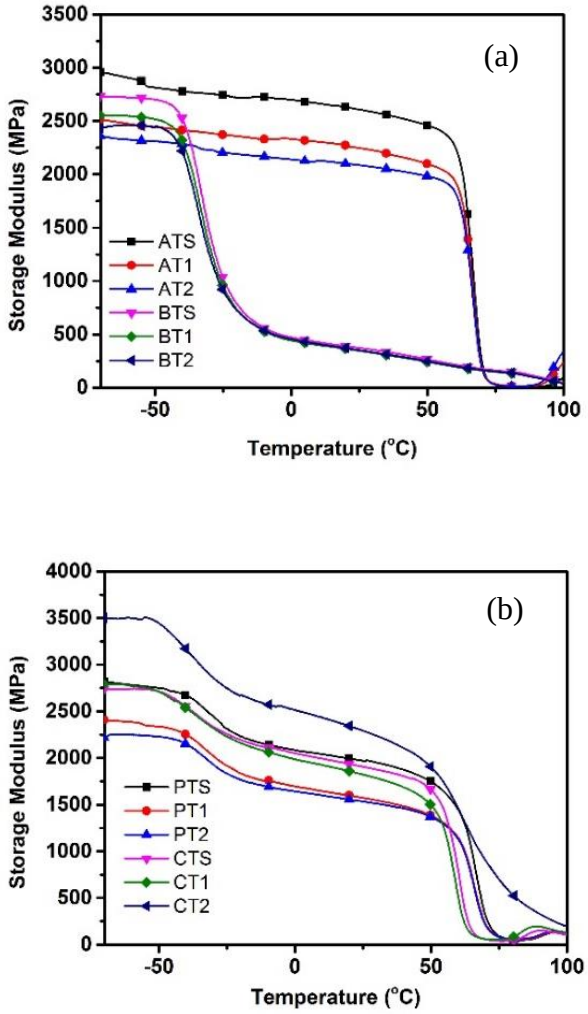

Figure 6.2: Storage modulus of talc base (a) pure and (b) blends compositions

Microcellular samples of PLA-PBSA-Talc (PT1 and PT2) exhibited a slightly lower storage modulus of 2930 MPa compared PLA-PBSA-TPP-Talc (CT2) which incidentally showed the highest storage modulus among all the compositions. This may be attributed to the bimodal structure exhibited by this particular blend. Figures 6.3 and 6.4 show tan δ curves of all specimens while Table 6.1 details values of T_g and tan δ for all solid and microcellular samples. Tan δ is the ratio between loss modulus and storage

modulus. In the tan δ curve, a peak is observed in the region where the rate of decrease of storage modulus is higher than that of loss modulus with increase in temperature. Temperature corresponding to the tan δ peak is often considered to be the glass transition temperature (T_g) [60].

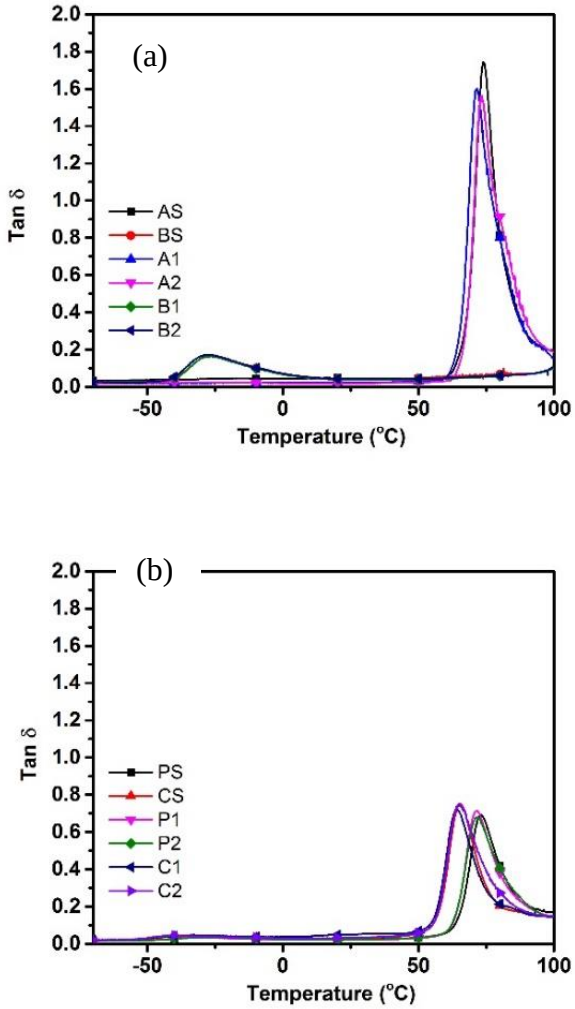

Figure 6.3 Temperature dependence of tan δ for (a) pure and (b) blends compositions

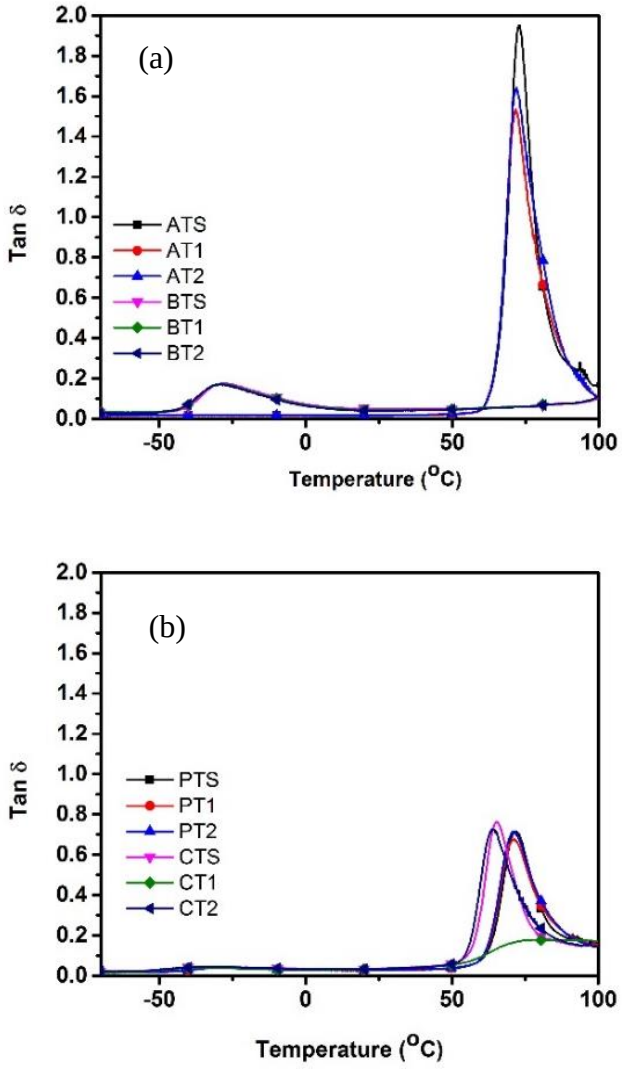

Figure 6.4: Temperature dependence of tan δ for talc based (a) pure and (b) blends compositions

As shown in Figure 6.3, T_g of PLA is approximately 75°C, which is contradictory to the general observation associated with this grade of PLA sourced from Natureworks; however, all trends observed in DSC and DMA remained the same. It can be seen that compatibilization led to a shift in tan δ peaks to slightly lower temperatures, i.e. TPP did compatibilize the blended systems. Interestingly the physical blend showed no glass

transition corresponding to PBSA, this may be due to the size and manner of PBSA dispersion. Addition of talc did not result in any significant shift in T_g based on tan δ peaks.

Sample	T_g (^oC)			Area under Tan δ		
	Solid	SCF1	SCF2	Solid	SCF1	SCF2
A	75.1	71.1	71.2	27.3	26.1	24.9
B	-27.4	-27.55	-27.35	9	9.9	10.9
P	72.9	71.7	71.8	11.6	12.17	12.35
C	64.5	64	63.7	12	13.5	13.4
AT	72	72.5	72.3	26.4	23.2	25.3
BT	-28.3	-28.7	-28.9	8.8	8.3	8.1
PT	71.2	71.4	71.8	12.48	12.9	12.9
CT	64.2	64	64	13.7	8.1	14.4

Table 6.1: Glass transition temperatures and area under tan δ for all compositions

The area under tan δ peak generally indicates that molecular chains exhibit a higher degree of mobility, thereby resulting in better damping ability [61]. For PLA (A) and PLA-Talc (AT) specimen, solid samples exhibited better damping properties than their microcellular counterparts, while PBSA and its talc counterparts also showed improvement in its damping properties. Addition of PBSA led to decline in damping in both physically and compatibilized blends. However, compositions exhibiting bimodality (C1, C2 and CT2) did show improvement in damping properties over their solid counterparts.

CHAPTER SEVEN

Physical and Mechanical Properties

Relative density of PLA, PBSA and all its blends were measured and documented in Table 7.1. Density reduction of 10 and 20 % was observed for pure PLA and pure PBSA samples, while density reduction of blends was similar to that of PLA. Generally, talc-based systems showed higher density compared to their non-talc counterparts, which can be attributed to the higher density of talc.

	Density (g/cm^3)				
	Solid	SCF		Solid	SCF
A	1.3	1.2	AT	1.4	1.2
B	1.3	1.1	BT	1.3	1.2
P	1.3	1.2	PT	1.3	1.2
C	1.3	1.2	CT	1.3	1.2

Table 7.1: Summary of densities of all compositions

Solid PLA showed the highest specific ultimate tensile strength (specific UTS) of 48.4 MPa/(g/cm^3) (Figure 7.1), while solid PBSA showed a specific ultimate tensile strength at half the value of PLA (18.8 MPa/(g/cm^3). Physical blending of PLA and PBSA led to the resultant blend exhibiting a specific UTS of 29.1 MPa/(g/cm^3), a value between that of the two constituent materials, and is in good agreement with earlier studies conducted by Eslami et al. [62]. In contrast, the compatibilized PLA/PBSA blend showed a lower specific UTS of 22.2 MPa/(g/cm^3),. Addition of talc led to slight decrease in the specific UTS values.

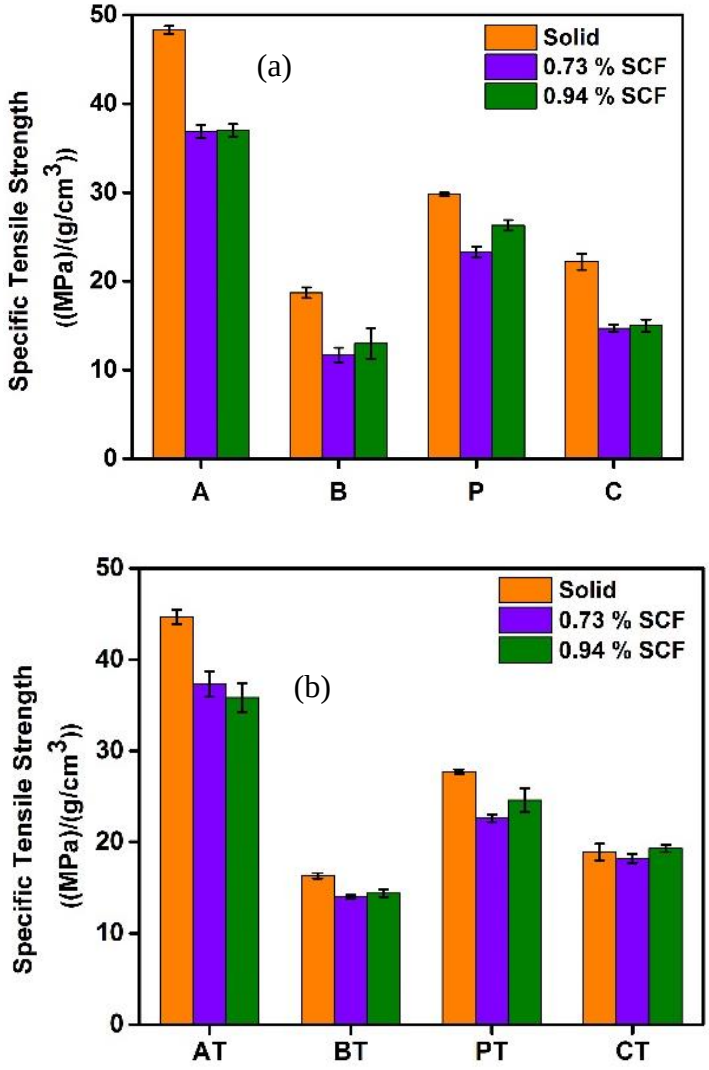

Figure 7.1: Specific Tensile Strength of (a) Non-Talc and (b) Talc Compositions

Addition of supercritical fluid was observed to lead to reduction in specific UTS compared to the corresponding solid compositions. Both SCF dosages – A1 and A2 – resulted in similar specific UTS values for pure PLA (36.3 and 36.9 MPa/(g/cm^3) respectively). A similar trend was observed in case of pure PBSA as well, with significantly lower values of specific UTS (11.8 and 13.0 MPa/(g/cm^3)) respectively). PLA/PBSA blends with SCF showed specific UTS values in the intermediate region between those of

pure PBSA and those of pure PLA, with compatibilization leading to a reduction in specific UTS values of blends (14.7 and 14.5 MPa/(g/cm^3) for dosages C1 and C2 respectively).

Addition of talc was observed to lead to an increase in specific UTS for AT1 samples from 36.9 MPa/(g/cm^3) for A1 to 37.3 MPa/(g/cm^3) for AT1, but a small reduction was observed for AT2 samples from 36.1 MPa/(g/cm^3) for A2 to 35.9 MPa/(g/cm^3) for AT2. Compositions BT1 and BT2 showed higher specific tensile strengths at 14.0 and 14.4 MPa/(g/cm^3) respectively, which might be due to the presence of uniform spherical cells and lower CDI value compared to their non-talc counterparts.

A significant increase was observed in specific UTS for the compatibilized compositions upon addition of talc – from 14.7 MPa (g/cm^3)) for C1 to 18.2 MPa/(g/cm^3) for CT1 and from 14.5 MPa/(g/cm^3) for C2 to 19.3 MPa/(g/cm^3) for CT2 respectively. This is possibly due to the occurrence of bimodal cell distribution, given the closeness of specific UTS values of both CT1 and CT2 compositions to that of the original solid composition, CTS, and the significant increase in specific UTS values upon the addition of talc. PT1 showed a specific UTS value of 22.7 MPa/(g/cm^3), showing reduction in specific UTS upon addition of talc, whereas PT2 showed the opposite trend with a higher specific UTS value of 28.4 MPa/(g/cm^3) compared to its corresponding solid composition. This may have been due to its higher cell density and finer pore size.

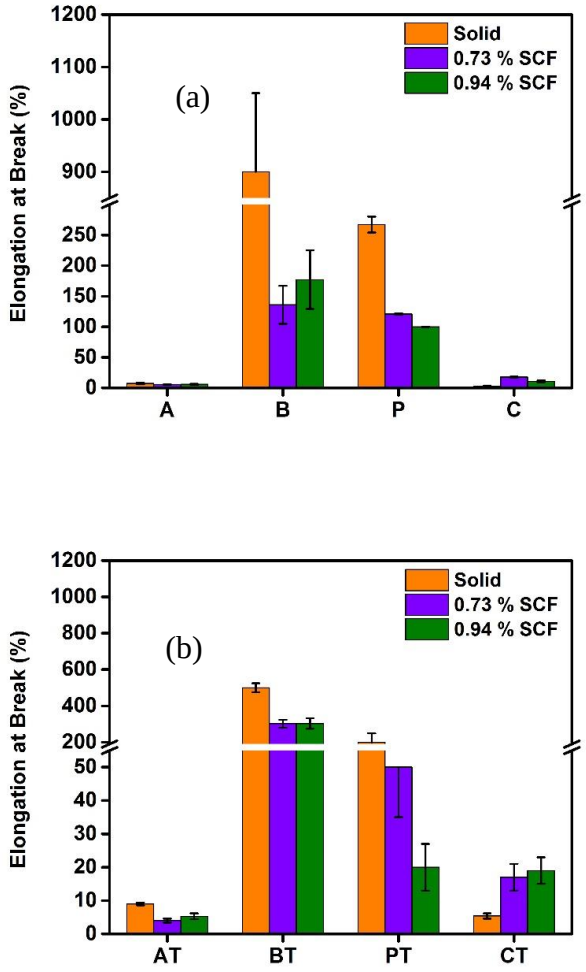

Figure 7.2: Elongation-at-Break for (a) Non-Talc and (b) Talc Compositions

Figure 7.2 shows elongation-at-break values obtained for pure polymers and blended compositions with and without the addition of talc. Elongation-at-break for PLA (AS) was reported as 7.5 %, more than an order of magnitude lower compared to that for PBSA (up to 917.0 %). Physical blending of PLA and PBSA yielded a material with an elongation-at-break between the two values, at 267.6 %, which was in good agreement with

similar studies conducted by Eslami et al.[62]. Notably, the compatibilized composition showed a higher elongation-at-break compared to PLA at 33.5 % (CS).

Introduction of SCF led to lowering of elongation-at-break (EB) for each composition. A1 and A2 had EB values of 5.5 % and 5.8 % respectively, slightly lower than those for AS. At the other end of the spectrum, EB values of B1 and B2 were at least 700 % lower than that of BS. PLA/PBSA physical blends P1 and P2 also had significant lowering of EB values at 121.6 % and 20.0 % respectively over their corresponding non-SCF blends. However, C1 and C2 proved an exception to this trend, with EB values at 17.8 % for C1 (over five-fold increase) and 10.9 % for C2 (three-fold increase) respectively.

Addition of talc produced a variety of impacts on EB values of compositions. EB of PLA was found to increase to 8.9 % in ATS while that of PBSA reduced to 510.6 % in case of BTS. PTS exhibited a lower elongation at break compared to PS at a value of 199.4 %, while a minor increase in EB value was observed for CS of 5.4 %.

Inclusion of talc in SCF compositions also led to exhibition of a number of trends. A1 and A2 showed slight reduction in EB to 4.8 % and 5.2 % for AT1 and AT2 samples respectively. However, EB values of B1 and B2 compositions nearly doubled, increasing to 302.5 % and 303.17 % for BT1 and BT2 respectively. Reduction was observed in EB values of physical blends – P1 and P2 – by 49.2 % and 18.4 % respectively. The compatibilized blends – CT1 and CT2 – showed higher EB values compared to their corresponding solid forms of CTS, with EB values of 17.7 % and 19.2 % respectively, which may have been due to the presence of bimodal structure.

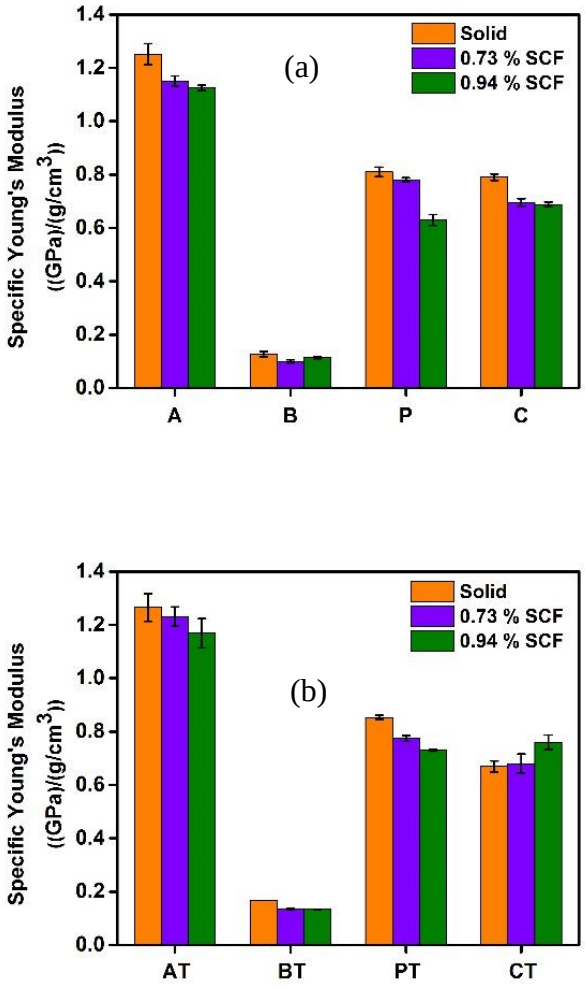

Figure 7.3: Specific Young's Modulus for (a) Non-Talc and (b) Talc Compositions

The highest value of specific Young's modulus among non-talc samples was observed for PLA (AS) at 1252 MPa/(g/cm^3) while the lowest was shown by pure PBSA (BS) at 128 MPa/(g/cm^3), nearly an order of magnitude lower (Figure 7.3). Physical blending of the two materials resulted in obtainment of specific Young's modulus of 816 MPa/(g/cm^3) (PS), while compatibilization led to further reduction in specific Young's modulus to 771 MPa/(g/cm^3)).

The effect of SCF addition on specific Young's modulus was minimal for most compositions. Slight reduction was observed in case of PLA (A1 – 1156 MPa/(g/cm^3); A2 – 1125 MPa/(g/cm^3)) and PBSA (B1 – 102 MPa/(g/cm^3); B2 – 113 MPa/(g/cm^3)) compared to AS and BS compositions respectively. The difference was found to be significant but in similar direction for physical blends (P1 – 787 MPA/(g/cm^3); P2 – 633 MPa/(g/cm^3)). However, the compatibilized blends showed a slightly larger decrease in specific Young's modulus of over 200 MPa/(g/cm^3) (C1 – 566 MPa/(g/cm^3); C2 – 538 MPa/(g/cm^3)).

Addition of talc was observed to result in a marginal increase in specific Young's modulus of all base compositions. ATS, BTS and PTS had slightly higher values of specific Young's modulus at 1266, 167 and 853 MPa/(g/cm^3) respectively. However, CTS showed the opposite trend with a lower specific Young's modulus value of 670 MPa(g/cm^3), a decrease of around 100 MPa/(g/cm^3) compared to its non-talc counterpart.

Additional varying effects were observed on specific Young's modulus of SCF compositions upon addition of talc. Increase was observed in values for PLA with SCF (AT1 – 1233 MPa/(g/cm^3), AT2 – 1168 MPa/(g/cm^3)) and for PBSA with SCF (BT1 – 134 MPa/(g/cm^3), BT2 – 133 MPa/(g/cm^3)). However, specific Young's modulus values were found to reduce for the physical blend PT1 (774 MPa/(g/cm^3)) and increase for PT2 (731 MPa/(g/cm3)), with these values being in close proximity to those for CT1 (712 MPa/(g/cm^3)) and CT2 (751 MPa/(g/cm^3)). Both CT1 and CT2 compositions showed a higher specific Young's modulus value compared to their corresponding solid form of CTS, possibly due to presence of bimodal cell distribution.

Specific toughness of PLA (AS) was determined to be 2.57 MPa/(g/cm^3), about 50-fold lower compared to that of PBSA (BS) at 129.48 MPa/(g/cm^3)), as can be seen in Figure 7.4. Physical blending of PLA and PBSA yielded a composition with specific toughness of 43.66 MPa/(g/cm^3) (PS), while the compatibilized blend yielded a lower specific toughness (0.42 MPa/(g/cm^3)) – the lowest of all specific toughness values.

Foamed PLA samples showed lower specific toughness values. A1 and A2 showed specific toughness values of 1.4 and 1.5 MPa/(g/cm^3) respectively, while values for B1 and B2 were 13.3 and 19.9 MPa/(g/cm^3) respectively. Specific toughness of non-compatibilized sample P1 showed a two-fold decrease to 18.11 MPa/(g/cm^3), while that of P2 showed a four-fold decrease to 3.6 MPa(g/cm^3)). Compatibilized blends showed the reverse trend with an increase in their specific toughness values to 1.5 and 0.9 MPa/(g/cm^3) respectively. This could be due to the presence of bimodal cellular distribution.

While specific toughness of talc filled PLA showed an increase to 3.0 MPa/(g/cm^3) (ATS), that of PBSA was found to halve to 66.0 MPa/(g/cm^3). Non-Compatibilized blends - PS also showed a reduction in specific toughness values compared to 30.4 MPa/(g/cm^3) in PTS, while a minor increase was observed in values for the compatibilized blends from 0.4 MPa/(g/cm^3) in CS to 0.6 MPa/(g/cm^3) in CTS.

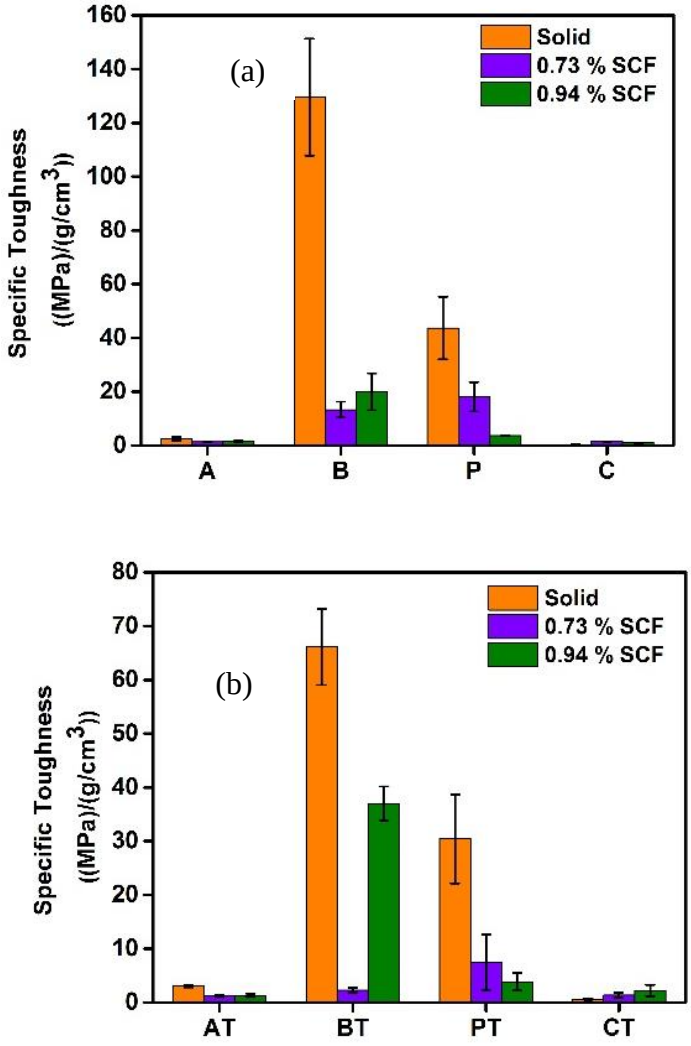

Figure 7.4: Specific Toughness for (a) Non-Talc and (b) Talc Compositions

Finally, addition of talc to SCF compositions showed a varying effect on specific toughness values as well. AT1 and AT2 showed lower specific toughness at 1.25 and 1.32 MPa/(g/cm^3) compared to A1 and A2 respectively, while BT1 and BT2 showed higher specific toughness at 37.0 and 37.0 MPa/(g/cm^3) compared to B1 and B2 respectively. Additionally, physical blend P1 showed a reduction to 7.4 MPa/(g/cm^3) while P2 showed

an increase in specific toughness to 3.8 MPa/(g/cm^3). The compatibilized blends showed the same trend as well, with C1 observing a reduction to 1.3 MPa/(g/cm^3) and C2 showing an increase to 2.2 MPa/(g/cm^3).

CHAPTER EIGHT

Conclusions and Future Work

In summary, addition of TPP in reactive melt-blending of PLA and PBSA showed a reduction in melt viscosity. Density reduction of 10 % and 20 % was observed for pure PLA and pure PBSA samples respectively, while most non-talc blends showed density reduction of 10 %. Addition of talc was observed to higher reduction in density due to obtainment of finer cell sizes, especially in case of PBSA where addition of talc led to more uniform spherical cells with highly regular cellular distribution.

Foaming of blends containing TPP led to obtainment of a bimodal cellular structure. This was attributed to multiple factors, such as:

a) TPP lowering melt viscosity
b) Lower melt viscosity contributing to a greater change in pore radius with time with respect to different generations of cell growth, and
c) Hierarchical or co-continuous blend architecture serving as nucleation sites for multimodal cellular distributions

In contrast, physical blends did not demonstrate bimodality, which might be due to higher melt strength, which in turn led to a more uniform cell growth, and presence of several nucleation sites at the interface of the blends for nucleation to occur, which in turn disrupted segregated foaming occurring within these polymers. Blended foams which exhibited bimodal structure also exhibited higher storage modulus and greater toughness compared to their foamed counterparts.

This study however can be taken to its final conclusion only through future work on a fundamental understanding of the effect of interfacial energy of physical and compatibilized blends and their correlation with SCF injection molding. Another potential area of work is to understand the effect of various process parameters with regard to obtaining multimodal cellular distributions with controlled cell size. A systematic study of ternary blends is also required in order to understand the different foaming mechanisms and how they can be used to possibly achieve bimodal cell distribution.

APPENDICES

APPENDIX A

Appendix A summarizes the average cell diameter and cell density of all compositions

Sample	Cell diameter (μm)		Cell Density (cells/mm^2)	Cell diameter (μm)		Cell Density (cells/mm^2)
	Average	Standard deviation		Average	Standard deviation	
A	52.1	12.7	1.59225E6	41.5	5.4	1.1E7
B	78.0	18.9	5.66247E6	70.2	17.0	7.7E6
P	43.7	11.34	6.03809E6	18.0	4.1	4.3E7
C	32.6	11.1	1.41978E7	25.03	8.6	1.10E7

Table AA.1: Cell size and cell density of non-talc filled microcellular injection molded PLA (A), PBSA (B), PLA-PBSA (P) and PLA-PBSA-TPP (C)

Sample	Cell diameter (μm)		Cell Density (cells/mm^2)	Cell diameter (μm)		Cell Density (cells/mm^2)
	Average	Standard deviation		Average	Standard deviation	
AT	47.9	22.5	7.30E6	33.	14.6	1.53E7
BT	90.8	15.5	1.28E6	43.5	14.6	1.04E6
PT	39.8	13	1.289E6	29.3	9.53	1.07E7
CT	180.5	18.4	1.08E6	17.5	4.3	2.46E7

Table AA.2 Cell size and cell density of talc filled microcellular injection molded PLA (AT), PBSA (BT), PLA-PBSA (PT) and PLA-PBSA-TPP (CT)

APPENDIX B

Appendix B graphically represents the probability distributions of cell diameter for all compositions

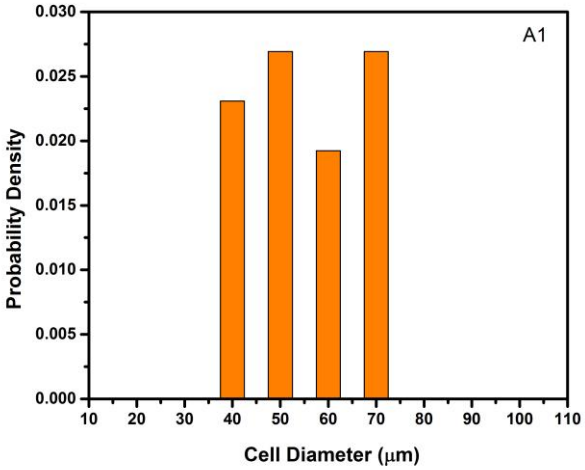

Figure AB.1: Probability distribution of cell diameter for A1

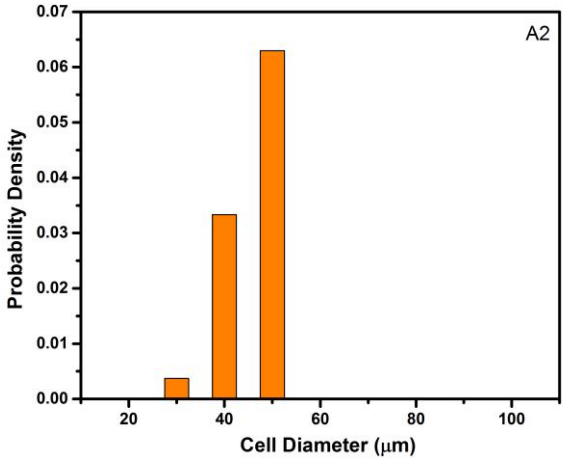

Figure AB.2: Probability distribution of cell diameter for A2

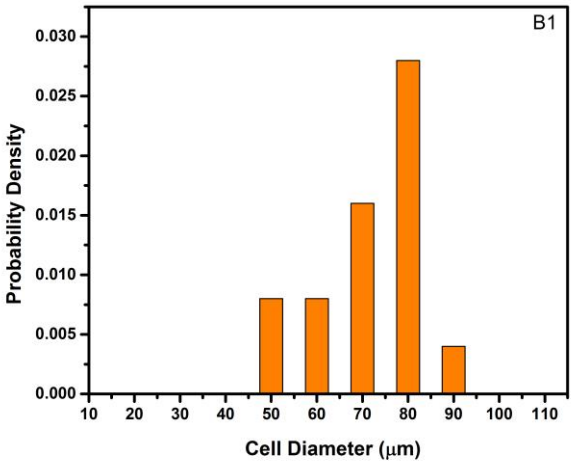

Figure AB.3: Probability distribution of cell diameter for B1

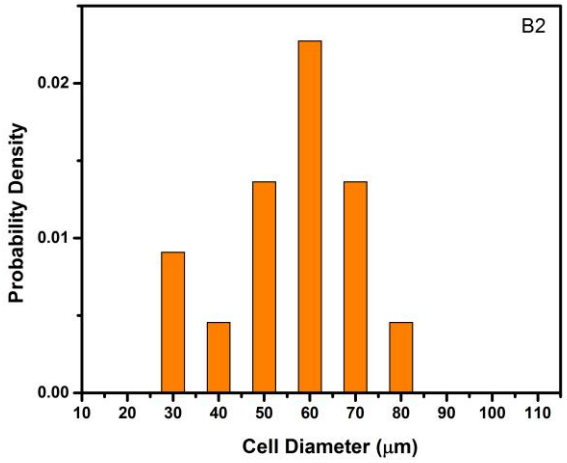

Figure AB.4: Probability distribution of cell diameter for B2

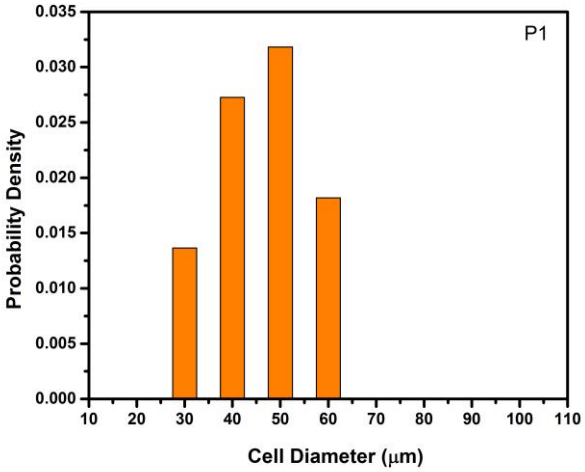

Figure AB.5: Probability distribution of cell diameter for P1

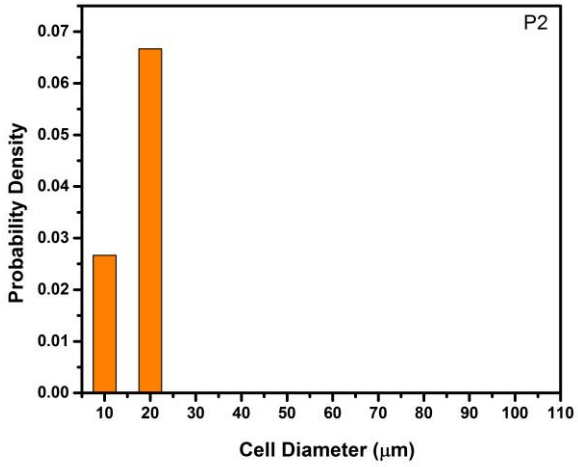

Figure AB.6: Probability distribution of cell diameter for P2

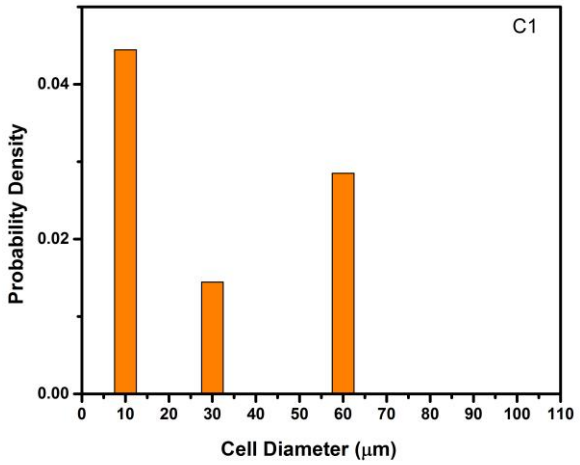

Figure AB.7: Probability distribution of cell diameter for C1

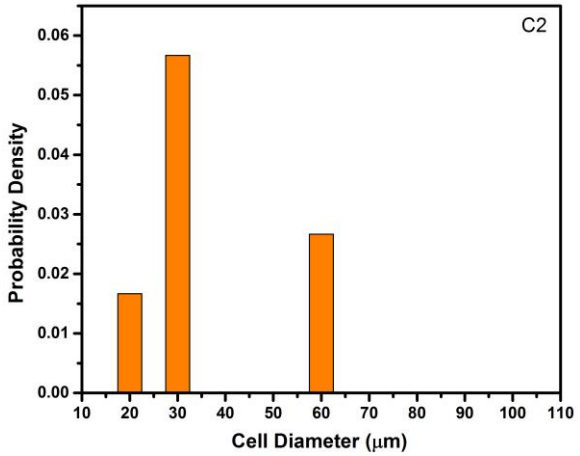

Figure AB.8: Probability distribution of cell diameter for C2

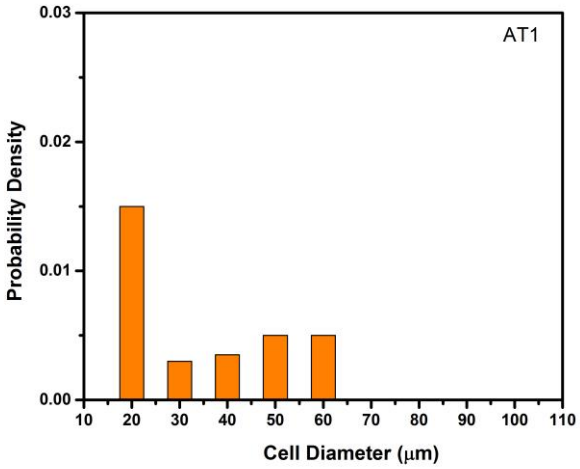

Figure AB.9: Probability distribution of cell diameter for AT1

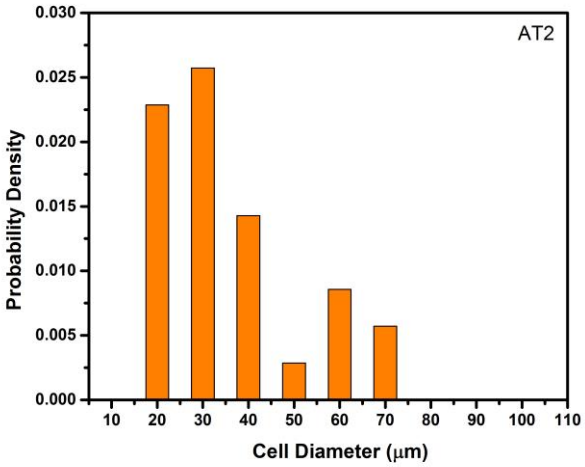

Figure AB.10: Probability distribution of cell diameter for AT2

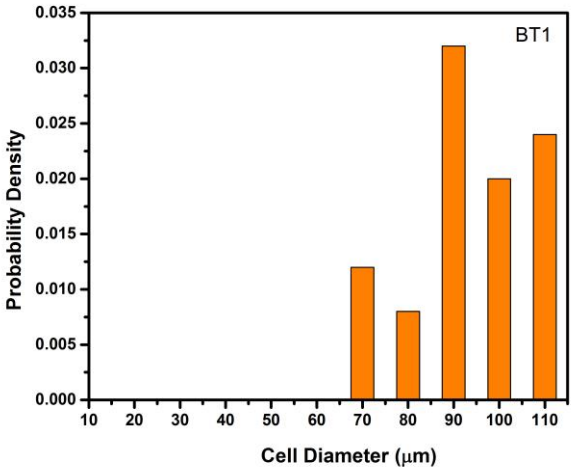

Figure AB.11: Probability distribution of cell diameter for BT1

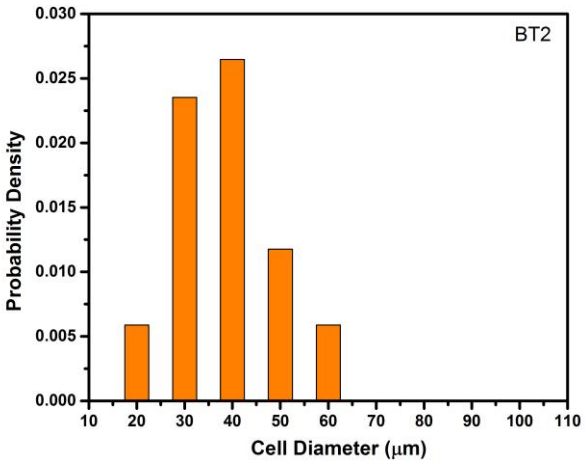

Figure AB.12: Probability distribution of cell diameter for BT2

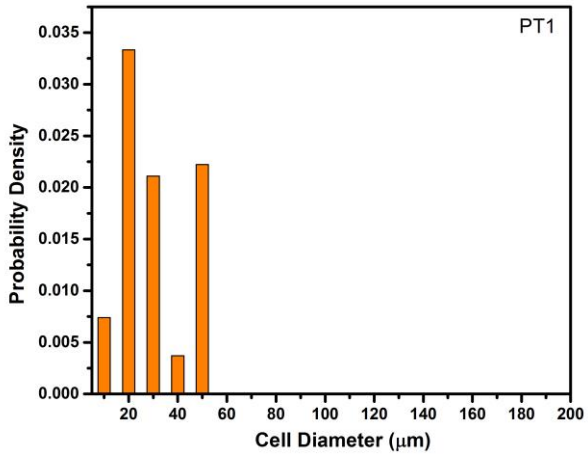

Figure AB.13: Probability distribution of cell diameter for PT1

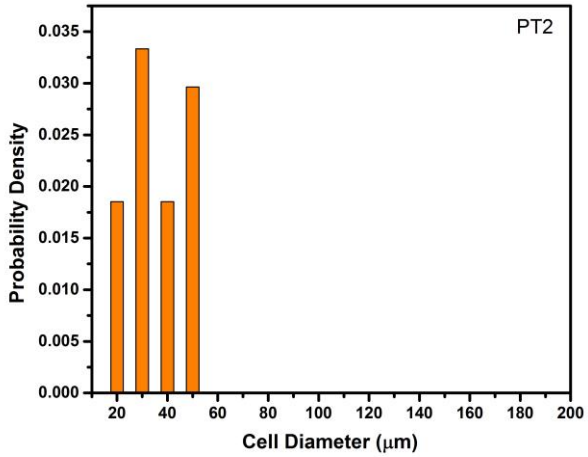

Figure AB.14: Probability distribution of cell diameter for PT2

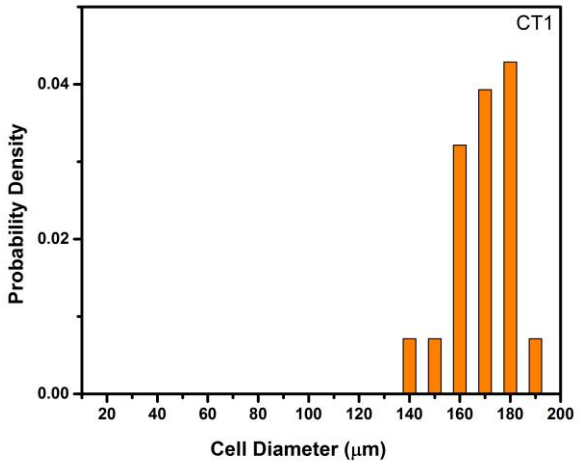

Figure AB.15: Probability distribution of cell diameter for CT1

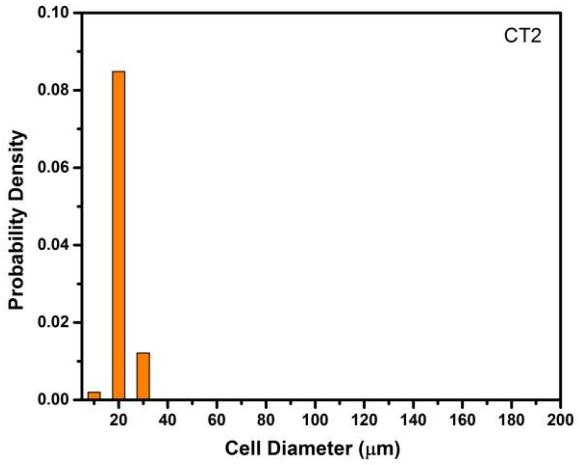

Figure AB.16: Probability distribution of cell diameter for CT2

APPENDIX C

Appendix C tabulates the mechanical properties for all compositions

Sample	Solid		SCF1		SCF2	
	Average	Standard deviation	Average	Standard deviation	Average	Standard deviation
A	48.3	0.45	36.9	0.71	37	0.704
B	18.7	0.6	11.7	0.8	13	1.7
P	29.8	0.2	23.3	0.6	26.3	0.6
C	22.2	0.9	14.7	0.4	15	0.7

Table AC.1- Specific ultimate tensile strength for non-talc samples

Sample	Solid		SCF2		SCF2	
	Average	Standard deviation	Average	Standard deviation	Average	Standard deviation
AT	44.68	0.8	37.31	1.4	35.81	1.6
BT	16.3	0.3	14	0.2	14.4	0.4
PT	27.7	0.23	22.6	0.4	24.6	1.3
CT	18.9	0.9	18.2	1.4	19.3	0.4

Table AC.2- Specific ultimate tensile strength for talc samples

Sample	Solid		SCF2		SCF2	
	Average	Standard deviation	Average	Standard deviation	Average	Standard deviation
A	7.5	1.4	5.5	0.38	5.82	0.79
B	900	150	136	31	177	48
P	267	13	121	0.8	100	0.27
C	3.35	0.6	17.8	0.7	10.96	1.4

Table AC.3-Elongation at break for non-talc samples

Sample	Solid	SCF2	SCF2

	Average	Standard deviation	Average	Standard deviation	Average	Standard deviation
AT	9	0.4	4	0.6	5.3	0.9
BT	500	25	302	22	303	29
PT	199	50	50	15	20	7
CT	5.4	0.8	17	4	19	4

Table AC.4-Elongation at break for talc samples

Sample	Solid		SCF2		SCF2	
	Average	Standard deviation	Average	Standard deviation	Average	Standard deviation
A	2.569	0.649	1.429	0.121	1.497	0.263
B	129.483	21.742	13.324	2.949	19.99	6.891
P	43.66	11.639	18.106	20.444	3.631	0.042
C	0.424	0.056	1.541	0.058	0.98	0.089

Table AC.5-Specific toughness for non-talc samples

Sample	Solid		SCF2		SCF2	
	Average	Standard deviation	Average	Standard deviation	Average	Standard deviation
AT	2.996	0.156	1.246	0.242	1.324	0.33
BT	66.085	--	37.064	3.494	37.014	3.147
PT	30.414	18.254	7.492	5.146	3.877	1.622
CT	0.662	0.137	1.37	0.461	2.245	1.056

Table AC.6-Specific toughness for talc samples

Sample	Solid		SCF2		SCF2	
	Average	Standard deviation	Average	Standard deviation	Average	Standard deviation
A	10251	0.04	1.15	0.02	1.125	0.01
B	0.127	0.01	0.1	0.006	0.113	0.003
P	0.81	0.018	0.78	0.008	0.63	0.02
C	0.771	0.012	0.566	0.014	0.538	0.009

Table AC.7- Specific Young’s modulus for non-talc samples

Sample	Solid		SCF2		SCF2	
	Average	Standard deviation	Average	Standard deviation	Average	Standard deviation
AT	1.265	0.051	1.232	0.035	1.168	0.055
BT	0.167		0.134	0.003	0.133	8E-4
PT	0.853	0.008	0.774	0.011	0.73	0.003
CT	0.669	0.021	0.711	0.057	0.75	0.027

Table AC.8- Specific Young's modulus for talc samples

REFERENCES

[1] U. EPA, Regulations and Standards: Light-Duty | Transportation and Climate, (n.d.). http://www.epa.gov/oms/climate/regs-light-duty.htm (accessed June 19, 2015).

[2] V. Nagarajan, A.K. Mohanty, M. Misra, Perspective on Polylactic Acid (PLA) based Sustainable Materials for Durable Applications: Focus on Toughness and Heat Resistance, (2016).

[3] A.H. Landrock, Handbook of plastic foams: types, properties, manufacture and applications, Elsevier, 1995.

[4] M.B. Gadi, Materials for Energy Efficiency and Thermal Comfort in Buildings, Mater. Energy Effic. Therm. Comf. Build. (2010) 681–708. doi:10.1533/9781845699277.3.681.

[5] M.J. Howard, Foams, edition 2, Desk-Top Data Bank, 1980.

[6] W. Michaeli, A. Cramer, L. Flórez, Processes and Process Analysis of Foam Injection Molding with Physical Blowing Agents, in: Polym. Foam., CRC Press, 2008: pp. 101–142.

[7] H. Guanghong, W. Yue, Microcellular Foam Injection Molding Process, (2012). doi:10.5772/34513.

[8] Sung W. Cha Nam P. Suh Daniel F. Baldwin Chul B. Park, Microcellular thermoplastic foamed with supercritical fluid, US5158986A, 1992. https://patents.google.com/patent/US5158986A/en.

[9] H. Urayama, T. Kanamori, Y. Kimura, Properties and Biodegradability of Polymer

Blends of Poly(L-lactide)s with Different Optical Purity of the Lactate Units, Macromol. Mater. Eng. 287 (2002) 116–121. doi:10.1002/1439-2054(20020201)287:2<116::AID-MAME116>3.0.CO;2-Z.

[10] H. Urayama, C. Ma, Y. Kimura, Mechanical and Thermal Properties of Poly(L-lactide) Incorporating Various Inorganic Fillers with Particle and Whisker Shapes, Macromol. Mater. Eng. 288 (2003) 562–568. doi:10.1002/mame.200350004.

[11] N.E. Suyatma, A. Copinet, L. Tighzert, V. Coma, Mechanical and Barrier Properties of Biodegradable Films Made from Chitosan and Poly (Lactic Acid) Blends, J. Polym. Environ. 12 (2004) 1–6. doi:10.1023/B:JOOE.0000003121.12800.4e.

[12] R.A. Auras, B. Harte, S. Selke, R. Hernandez, Mechanical, Physical, and Barrier Properties of Poly(Lactide) Films, J. Plast. Film Sheeting. 19 (2003) 123–135. doi:10.1177/8756087903039702.

[13] J. Odent, J.-M. Raquez, P. Dubois, Highly Toughened Polylactide-Based Materials through Melt-Blending Techniques, in: Biodegrad. Polyesters, Wiley-VCH Verlag GmbH & Co. KGaA, Weinheim, Germany, 2015: pp. 235–274. doi:10.1002/9783527656950.ch10.

[14] J.-B. Zeng, K.-A. Li, A.-K. Du, M.M. Reddy, S. Vivekanandhan, M. Misra, et al., Compatibilization strategies in poly(lactic acid)-based blends, RSC Adv. 5 (2015) 32546–32565. doi:10.1039/C5RA01655J.

[15] G. Kfoury, J.-M. Raquez, F. Hassouna, J. Odent, V. Toniazzo, D. Ruch, et al., Recent advances in high performance poly(lactide): from “green” plasticization to

super-tough materials via (reactive) compounding, Front. Chem. 1 (2013) 32. doi:10.3389/fchem.2013.00032.

[16] L. Jiang, M.P. Wolcott, J. Zhang, Study of biodegradable polylactide/poly(butylene adipate-co-terephthalate) blends., Biomacromolecules. 7 (2006) 199–207. doi:10.1021/bm050581q.

[17] T. Yokohara, M. Yamaguchi, Structure and properties for biomass-based polyester blends of PLA and PBS, Eur. Polym. J. 44 (2008) 677–685. doi:10.1016/j.eurpolymj.2008.01.008.

[18] M. Zhang, N.L. Thomas, Blending polylactic acid with polyhydroxybutyrate: The effect on thermal, mechanical, and biodegradation properties, Adv. Polym. Technol. 30 (2011) 67–79. doi:10.1002/adv.20235.

[19] H. Zhao, Z. Cui, X. Sun, L.-S. Turng, X. Peng, Morphology and Properties of Injection Molded Solid and Microcellular Polylactic Acid/Polyhydroxybutyrate-Valerate (PLA/PHBV) Blends, Ind. Eng. Chem. Res. 52 (2013) 2569–2581. doi:10.1021/ie301573y.

[20] L. Wang, W. Ma, R.A. Gross, S.P. McCarthy, Reactive compatibilization of biodegradable blends of poly(lactic acid) and poly(ε-caprolactone), Polym. Degrad. Stab. 59 (1998) 161–168. doi:10.1016/S0141-3910(97)00196-1.

[21] V. Ojijo, S.S. Ray, R. Sadiku, Toughening of biodegradable polylactide/poly(butylene succinate-co-adipate) blends via in situ reactive compatibilization., ACS Appl. Mater. Interfaces. 5 (2013) 4266–76. doi:10.1021/am400482f.

[22] H. Eslami, M.R. Kamal, Effect of a chain extender on the rheological and mechanical properties of biodegradable poly(lactic acid)/poly[(butylene succinate)- co -adipate] blends, J. Appl. Polym. Sci. 129 (2013) 2418–2428. doi:10.1002/app.38449.

[23] M. Sauceau, J. Fages, A. Common, C. Nikitine, E. Rodier, New challenges in polymer foaming: A review of extrusion processes assisted by supercritical carbon dioxide, Prog. Polym. Sci. 36 (2011) 749–766. doi:10.1016/j.progpolymsci.2010.12.004.

[24] J. Wang, W. Zhu, H. Zhang, C.B. Park, Continuous processing of low-density, microcellular poly(lactic acid) foams with controlled cell morphology and crystallinity, Chem. Eng. Sci. 75 (2012) 390–399. doi:10.1016/j.ces.2012.02.051.

[25] S. Pilla, A. Kramschuster, L. Yang, J. Lee, S. Gong, L.-S. Turng, Microcellular injection-molding of polylactide with chain-extender, Mater. Sci. Eng. C. 29 (2009) 1258–1265. doi:10.1016/j.msec.2008.10.027.

[26] F.H. Gojny, J. Nastalczyk, Z. Roslaniec, K. Schulte, Surface modified multi-walled carbon nanotubes in CNT/epoxy-composites, Chem. Phys. Lett. 370 (2003) 820–824. doi:10.1016/S0009-2614(03)00187-8.

[27] Flexible bimodal foam structures, (1993).

[28] Z. Ma, G. Zhang, Q. Yang, X. Shi, A. Shi, Fabrication of microcellular polycarbonate foams with unimodal or bimodal cell-size distributions using supercritical carbon dioxide as a blowing agent, J. Cell. Plast. 50 (2013) 55–79. doi:10.1177/0021955X13503849.

[29] X. Shi, G. Zhang, Y. Liu, Z. Ma, Z. Jing, X. Fan, Microcellular foaming of polylactide and poly(butylene adipate-co-terphathalate) blends and their $CaCO_3$ reinforced nanocomposites using supercritical carbon dioxide, Polym. Adv. Technol. 27 (2016) 550–560. doi:10.1002/pat.3768.

[30] C. Zhang, B. Zhu, D. Li, L.J. Lee, Extruded polystyrene foams with bimodal cell morphology, Polymer (Guildf). 53 (2012) 2435–2442. doi:10.1016/j.polymer.2012.04.006.

[31] A. Ameli, D. Jahani, M. Nofar, P.U. Jung, C.B. Park, Development of high void fraction polylactide composite foams using injection molding: Mechanical and thermal insulation properties, Compos. Sci. Technol. 90 (2014) 88–95. doi:10.1016/j.compscitech.2013.10.019.

[32] A. Wong, C.B. Park, The effects of extensional stresses on the foamability of polystyrene–talc composites blown with carbon dioxide, Chem. Eng. Sci. 75 (2012) 49–62. doi:10.1016/j.ces.2012.02.040.

[33] S.N. Leung, A. Wong, L.C. Wang, C.B. Park, Mechanism of extensional stress-induced cell formation in polymeric foaming processes with the presence of nucleating agents, J. Supercrit. Fluids. 63 (2012) 187–198. doi:10.1016/j.supflu.2011.12.018.

[34] H.A. Kharbas, T. Ellingham, M. Manitiu, G. Scholz, L.-S. Turng, Effect of a cross-linking agent on the foamability of microcellular injection molded thermoplastic polyurethane, J. Cell. Plast. (2016) 0021955X16652109. doi:10.1177/0021955X16652109.

[35] Chemical Foaming Agent Extrusion Processing Guide, (n.d.). http://www.bergeninternational.com/extrusion-extruding-chemical-foaming-agents-plastics-processing-guide.php.

[36] S. Pilla, A. Kramschuster, J. Lee, C. Clemons, S. Gong, L.-S. Turng, Microcellular processing of polylactide–hyperbranched polyester–nanoclay composites, J. Mater. Sci. 45 (2010) 2732–2746. doi:10.1007/s10853-010-4261-6.

[37] B. Jacques, J. Devaux, R. Legras, E. Nield, Reactions induced by triphenyl phosphite addition during melt mixing of PET/PBT blends: chromatographic evidence of a molecular weight increase due to the creation of bonds of two different natures, Polymer (Guildf). 38 (1997) 5367–5377. doi:10.1016/S0032-3861(97)00097-9.

[38] S.M. Aharoni, C.E. Forbes, W.B. Hammond, D.M. Hindenlang, F. Mares, K. O'Brien, et al., High-temperature reactions of hydroxyl and carboxyl PET chain end groups in the presence of aromatic phosphite, J. Polym. Sci. Part A Polym. Chem. 24 (1986) 1281–1296. doi:10.1002/pola.1986.080240614.

[39] M. Kutz, Handbook of environmental degradation of materials, William Andrew /Elsevier, 2012.

[40] J. Odent, P. Leclère, Toughening of polylactide by tailoring phase-morphology with P[CL-co-LA] random copolyesters as biodegradable impact modifiers, Eur. Polym. J. 49 (2013) 914–922. doi:10.1016/j.eurpolymj.2012.12.006.

[41] A.L.N. Silva, T.F. Cipriano, ntonio H.M. da F.T. da ASilva, M.C.C.G. Rocha, A.F. Sousa, G.M. da Silva, Thermal, rheological and morphological properties of

poly (lactic acid) (PLA) and talc composites, Polímeros Ciência E Tecnol. 24 (2014) 276–282. doi:10.4322/polimeros.2014.067.

[42] F. Yu, T. Liu, X. Zhao, X. Yu, A. Lu, J. Wang, Effects of talc on the mechanical and thermal properties of polylactide, J. Appl. Polym. Sci. 125 (2012) E99–E109. doi:10.1002/app.36260.

[43] S. Jain, M. Misra, A.K. Mohanty, A.K. Ghosh, Thermal, Mechanical and Rheological Behavior of Poly(lactic acid)/Talc Composites, J. Polym. Environ. 20 (2012) 1027–1037. doi:10.1007/s10924-012-0500-z.

[44] H.A. Kharbas, T. Ellingham, M. Manitiu, G. Scholz, L.-S. Turng, Effect of a cross-linking agent on the foamability of microcellular injection molded thermoplastic polyurethane, J. Cell. Plast. (2016) 0021955X16652109. doi:10.1177/0021955X16652109.

[45] J. Meissner, Polymer melt elongation?methods, results, and recent developments, Polym. Eng. Sci. 27 (1987) 537–546. doi:10.1002/pen.760270802.

[46] V. Ojijo, H. Cele, S. Sinha Ray, Morphology and Properties of Polymer Composites Based on Biodegradable Polylactide/Poly[(butylene succinate)-co-adipate] Blend and Nanoclay, Macromol. Mater. Eng. 296 (2011) 865–877. doi:10.1002/mame.201100042.

[47] X. Yang, H. Xu, K. Odelius, M. Hakkarainen, Poly(lactide)-g-poly(butylene succinate-co-adipate) with High Crystallization Capacity and Migration Resistance, Materials (Basel). 9 (2016) 313. doi:10.3390/ma9050313.

[48] S.H.P. Bettini, M.P.P. de Miranda Josefovich, P.A.R. Muñoz, C. Lotti, L.H.C.

Mattoso, Effect of lubricant on mechanical and rheological properties of compatibilized PP/sawdust composites, Carbohydr. Polym. 94 (2013) 800–806. doi:10.1016/j.carbpol.2013.01.080.

[49] S. Pilla, A. Kramschuster, L. Yang, J. Lee, S. Gong, L.-S. Turng, Microcellular injection-molding of polylactide with chain-extender, Mater. Sci. Eng. C. 29 (2009) 1258–1265. doi:10.1016/j.msec.2008.10.027.

[50] G. Li, H. Li, L.S. Turng, S. Gong, C. Zhang, Measurement of gas solubility and diffusivity in polylactide, Fluid Phase Equilib. 246 (2006) 158–166. doi:10.1016/j.fluid.2006.05.030.

[51] F.J. Gomez-Gomez, D. Arencon, M.A. Sanchez-Soto, A.B. Martinez, Influence of the injection moulding parameters on the microstructure and thermal properties of microcellular polyethylene terephthalate glycol foams, J. Cell. Plast. 49 (2013) 47–63. doi:10.1177/0021955X12460044.

[52] L.J. Lee, C. Zeng, X. Cao, X. Han, J. Shen, G. Xu, Polymer nanocomposite foams, Compos. Sci. Technol. 65 (2005) 2344–2363. doi:10.1016/j.compscitech.2005.06.016.

[53] Y. Moon, S.W. Cha, Study on viscosity changes with talc in microcellular foaming process, Fibers Polym. 8 (2007) 393–398. doi:10.1007/BF02875828.

[54] S. Yetgin, H. Unal, A. Mimaroglu, Influence of foam agent content and talc filler on the microcellular and mechanical properties of injection molded polypropylene and talc filled polypropylene composite foams, J. Cell. Plast. 50 (2014) 563–576. doi:10.1177/0021955X14543313.

[55] S. Rizvi, M. Alaei, A. Yadav, N. Bhatnagar, Quantitative analysis of cell distribution in injection molded microcellular foam, J. Cell. Plast. 50 (2014) 199–219. doi:10.1177/0021955X14524081.

[56] S. Rizvi, M. Alaei, A. Yadav, N. Bhatnagar, Quantitative analysis of cell distribution in injection molded microcellular foam, J. Cell. Plast. 50 (2014) 199–219. doi:10.1177/0021955X14524081.

[57] G. Dong, G. Zhao, Y. Guan, S. Li, X. Wang, Formation mechanism and structural characteristics of unfoamed skin layer in microcellular injection-molded parts, J. Cell. Plast. 52 (2016) 419–439. doi:10.1177/0021955X15577149.

[58] A.C. Fowlks, R. Narayan, The effect of maleated polylactic acid (PLA) as an interfacial modifier in PLA-talc composites, J. Appl. Polym. Sci. 118 (2010) 2810–2820. doi:10.1002/app.32380.

[59] B.L. Shah, L.M. Matuana, P.A. Heiden, Novel coupling agents for PVC/wood-flour composites, J. Vinyl Addit. Technol. 11 (2005) 160–165. doi:10.1002/vnl.20056.

[60] S. Pilla, A. Kramschuster, J. Lee, G.K. Auer, S. Gong, L.-S. Turng, Microcellular and Solid Polylactide–Flax Fiber Composites, Compos. Interfaces. 16 (2009) 869–890. doi:10.1163/092764409X12477467990283.

[61] A. Javadi, A.J. Kramschuster, S. Pilla, J. Lee, S. Gong, L.-S. Turng, Processing and characterization of microcellular PHBV/PBAT blends, Polym. Eng. Sci. 50 (2010) 1440–1448. doi:10.1002/pen.21661.

[62] H. Eslami, M.R. Kamal, Elongational Rheology and Mechanical Properties of

Biodegradable Pla / Pbsa Blends, (n.d.) 3–6.